CHALMERS
UNIVERSITY OF TECHNOLOGY

CFD Method Validation: Simulation of Defroster Performance Testing

Master's thesis in Mechanics and Maritime Sciences

ISAREE JIRATTHITICHEEP

Department of Mechanics and Maritime Sciences
CHALMERS UNIVERSITY OF TECHNOLOGY
Gothenburg, Sweden 2020

MASTER'S THESIS IN MECHANICS AND MARITIME SCIENCES

CFD Method Validation: Simulation of Defroster Performance Testing

ISAREE JIRATTHITICHEEP

Department of Mechanics and Maritime Sciences
Division of Fluid Dynamics
CHALMERS UNIVERSITY OF TECHNOLOGY
Göteborg, Sweden 2020

CFD Method Validation: Simulation of Defroster Performance Testing
ISAREE JIRATTHITICHEEP

Master's Thesis 2020:77
Department of Mechanics and Maritime Sciences
Division of Fluid Dynamics
Chalmers University of Technology
SE-412 96 Göteborg
Sweden
Telephone: + 46 (0)31-772 1000

Cover:
Volvo VA ice melting pattern on the Windscreen and front side windows from the simulation with proper settings at 16-minute testing time similar to the one illustrated in Figure 4.14.

Department of Mechanics and Maritime Sciences
Göteborg, Sweden 2020-10-28

CFD Method Validation: Simulation of Defroster Performance Testing
Master's thesis in Mechanic and Maritime Sciences
ISAREE JIRATTHITICHEEP
Department of Mechanics and Maritime Sciences
Division of Fluid Dynamics
Chalmers University of Technology

Abstract

An accurate prediction of the ice melting pattern would be useful for the performance evaluation and energy optimization during the design phase of the vehicle defroster. It can also be used to ensure that the design passes the legal requirement as well. A transient CFD simulation method suitable for defroster performance simulation is therefore verified and validated in this study. The aim is to achieve as accurate and efficient simulation as possible for the use in industry. In this study, the geometry is first prepared in ANSA and the simulation and post-processing are executed in STAR-CCM+. Fluid film model is used to model the ice layer on the windscreen and its melting and solidification model plays an important part in obtaining the ice melting pattern. The model is first verified regarding the optimal mesh setting, time step size, flow solver setting and the choice of turbulence models. It was found that the mesh and turbulence model can affect the simulation stability greatly. Realizable k-epsilon, k-epsilon Lag EB and SST k-omega model are examined and Realizable k-epsilon is selected as the most suitable one for this simulation. The time step size and flow solver can then be adjusted to maximize the solution efficiency. With steady state nature of the flow field, the time step size can be increased up to 5 or even 15 s depend on the required level of accuracy. With the flow solver frozen after a steady state initialization, the solver time per time step can be further reduced by 30 – 35%. With 15 s time step size, the 42 minutes testing time transient simulation can be executed within 2.5 hours with 960 computational cores and still yields results with acceptable accuracy. Next, to improve the result accuracy, boundary conditions and the domain geometry are validated against the test data. It was found that the velocity and turbulence profile at HVAC-defroster connection is needed to achieve accurate flow impingement pattern and ice melting pattern on the windscreen. The ice layer thickness can also affect the melting rate considerably so it should be verified in future tests. In contrast, it is apparent that the simulation is not too sensitive to the defroster inlet temperature profile and so a variation within 5 – 10 ℃ is acceptable for future application. With these verifications, highly accurate ice melting pattern is achieved for both the windscreen and front side windows at the end of this study. The application of this final scheme on another vehicle model also confirms the method reliability.

Key words: CFD, Defroster, Deicing, Fluid film model, Melting and solidification

Contents

Acknowledgement

This CFD simulation method development was executed in cooperation with the Climate CFD team at Volvo Cars, Sweden as a part of the VESC program during February to October 2020 through the COVID pandemic time. I would like to thank Gregor McKechnie, Sam Gullman and Tomas Dandenell, my supervisor and managers at Volvo Cars, for granting me this opportunity into the program and for continual support and guidance since my first day at the company. I also highly appreciate all the information provided by Sathyavanan Chinnaswamy and Vala Roshdi and of course all tips and interesting discussions I had with Erik Johansson, Alper Cesur, Anant Patwari and other colleagues in the team. Additionally, this work has also been done with excellent support from Mani Johannesson and Marian Gielmuda from STAR-CCM+ support team. Thank you for all the helpful answers and suggestions you provided. Finally, |I would like to thank Professor Srdjan Sasic for being my thesis examiner and guiding me through all stages of the project as well.

Göteborg October 2020-10-28

ISAREE JIRATTHITICHEEP

Notations

Variables

α	Elliptic blending factor		
α_s	Relative solid volume fraction		
β	Coefficient of thermal expansion		1/K
ε	Turbulent dissipation rate		m^2/s^3
λ	Thermal conductivity		W/mK
μ	Dynamic viscosity		kg/ms
μ_t	Turbulent viscosity		kg/ms
ν	Kinematic viscosity		m^2/s
ρ	Density		kg/m^3
σ	Stress tensor		N/m^2
τ	Shear stress tensor		N/m^2
τ_{RANS}	RANS stress tensor term		N/m^2
τ_w	Wall shear stress		N/m^2
τ_{wf}	Wall shear force		N/m^2
Υ_M	Compressibility modification term		W/m^3
ϕ	Transport variable		
φ	Normalized wall-normal stress component		
ω	Specific dissipation rate		1/s
C	Model coefficient [See Appendix]		
c_p	Specific heat capacity		J/kgK
E	Specific energy		J/kg
F_b	Body force per volume		N/m^3
G_ω	Specific dissipation production term		kg/m^3s^2
$G_{\omega D}$	Cross diffusion term		kg/m^3s^2
G_a	Additional production term		W/m^3
G_b	Buoyancy production term		W/m^3
G_k	Turbulent production term		W/m^3
g	Gravitational vector	9.81	m/s^2
H	Specific enthalpy		J/kg
H_{film}	Fluid film specific enthalpy		J/kg
H_{fus}	Enthalpy of fusion		J/kg
H_{sen}	Sensible enthalpy		J/kg
H_{static}	Static enthalpy		J/kg
h	Convective heat transfer coefficient		W/m^2K
$\mathbb{h}_{film}$	Film thickness		m
I	Identity matrix/tensor		
k	Turbulent kinetic energy		m^2/s^2
L	Characteristic length		m
l_ε	Length scale function		m
l_t	Turbulent length scale		m
M	Gas molecular weight		kg/kmol
M_t	Turbulent Mach number		
n	Wall normal direction vector		
p	Instantaneous pressure		Pa
P	Production term		
P_ε	of dissipation rate		W/m^3
P_φ	of the normalized wall-normal stress component		kg/m^3s
P_ω	of specific dissipation rate		kg/m^3s^2
P_k	of turbulent kinetic energy		W/m^3
Pr	Prandtl number		
$\mathrm{Pr_t}$	Turbulent Prandtl number		
$\dot{q}$	Heat flux vector		W/m^2
$\dot{q}_w$	Heat flux vector at wall		W/m^2
R_u	Universal gas constant	8314.4621	J/kmol K
Re_d	Wall distance Reynolds number		
S	Strain rate tensor		1/s
S	Sutherland's constant		K
T	Temperature		K
T_L	Liquidus temperature		K
T_S	Solidus temperature		K
T_w	Wall temperature		K
T^*	Normalized temperature		
T_∞	Reference temperature		
$\hat{T}_C$	Near-wall cell temperature		K
t	Time		s
t_t	Turbulent time scale		s
t_{te}	Large-eddy time scale		s
u^*	Velocity scale		m/s
u^+	Non-dimensional wall-tangential velocity vector		
u_τ	Wall friction velocity		m/s
v	Instantaneous velocity		m/s
v_c	Speed of sound		m/s
$v_{\parallel g}$	Velocity component parallel to the gravitational vector		m/s
$v_{\perp g}$	Velocity component perpendicular to the gravitational vector		m/s
$v_{\parallel w}$	Wall-tangential velocity vector		m/s
$\bar{\mathbf{W}}$	Mean vorticity tensor		1/s
y	Wall distance		m

Superscript

$\bar{\phi}$	Mean value
ϕ'	Fluctuating value
$\dot{\phi}$	Flux vector
$\hat{\phi}$	RANS averaged value
ϕ^+	Non-dimensional value

Subscript

i, j, k	Cartesian coordinate direction
$film$	Fluid film properties
t	Turbulent properties
w	Wall properties
KO	of k-omega model
LEB	of LEB k-epsilon model

Acronym

CFD	Computational fluid dynamic
CAD	Computer-aided design
EC	EU Commission
HTC	Heat transfer coefficient
HVAC	Heating, ventilation and air conditioning system
KE	k-epsilon model
KO	k-omega model
LEB	Lag Elliptic blending model
RANS	Reynolds averaged Navier-Stokes model
RKE	Realizable k-epsilon model
SKE	Standard k-epsilon model
SS	Steady state

1 Introduction

According to the EU Commission (EC) Regulation, defroster is a compulsory equipment for every vehicle sold or used within the European Union. To ensure sufficient visibility through the windshield in cold climate condition, the EC Regulation clearly defines an expected level of performance from the installed defroster. In other words, all model of motor vehicle shall pass a defrosting test done in specific conditions indicated in the EC Regulation before it can be approved to be used in EU.

However, this defroster testing is often possible later in the design phase when the sample model of the vehicle becomes available. Thus, this performance test is not only expensive, but also inefficient since the design is already locked in. This means although flaws are discovered during the test, little can be adjusted by then. Thus, CFD simulation of the defroster has become a compelling supplementary, if not an alternative, in the automotive industry. With the simulation, the design could be tested much faster and cheaper. It can also be tested much earlier in the design phase as well, and so more optimization can be done. With more efficient IC engine and electrical engine, heat supply has become a scarce resource in the modern vehicle. The defroster could consume up to 7 – 10 kW of energy during maximum heating scenario and therefore, its energy optimization is significant. With the simulation, the most efficient inlet conditions can be found so that, the defroster can remove the ice within regulation time while using the lowest energy possible as well.

At Volvo Cars, currently the defroster is still tested solely with the physical test and there is only a steady state simulation method for the air flow distribution over the windscreen available, without the inclusion of any thermodynamics or transient defrosting phenomenon. Thus, only the air distribution pattern can be optimized during the design phrase, but not the energy consumption nor the defrosting time. Hence, it has become one of the company topics of interest to develop a simulation method for the full defrosting system as described above.

Furthermore, academically, defrosting simulation can be quite complex as well, as it involves different modes of heat transfer, transient phenomena of phase changing and the modelling of thin film that represents the ice layer. Moreover, there is the matter of ensuring both simulation efficiency and accuracy with phenomena with different time scales such as the flow field and the heat conduction as well. Thus, overall, this study seems appealing both in the industry and academic point of view.

With reasons stated above, this master thesis therefore aims to develop a reliable and efficient simulation method for modeling the defrosting on the windscreen and front side windows. The simulation should be able to model accurate air flow, temperature distribution and the ice melting pattern over the windscreen as well as predicting accurate defrosting time. In this study, several simulation settings, models, solvers, and boundary conditions are verified and validated with available test results. Finally, the simulation scheme reliability is also examined by testing it on another vehicle model as well. Note that vehicle model names are made anonymous in this report for the sake of confidentiality.

2 Literature Review

Computational fluid dynamics (CFD) deals with the modelling of fluid flow problems using numerical approaches. By solving for the local transport variables such as velocity, pressure and temperature in each discretized volume in the domain of interest, fluid flow characteristics can be tracked and visualized. This allows products and processes to be studied, evaluated and optimized with more details and efficiency compared to the convectional physical test.

To achieve these transport variables, various transport equations and models based on the physics of the fluid dynamics are solved. In this chapter, the main equations, models and their underlying assumptions involved in simulating defroster performance are reviewed. The chapter first lays out the governing transport equations for mass, momentum and energy, followed by the modelling of fluid film used to simulate the ice layer. Finally, different choices of the turbulence modelling in the air domain are discussed. Advantages and limitations of each model are also included to support the choice of models selected in this study.

2.1 Governing transport equations

The simulation of defroster performance essentially involves 3 aspects of modelling: the transport of mass, momentum and energy in the domain. 3 fundamental transport equations derived from the principle of mass, momentum and energy conservation are thus solved for each of these aspects. These governing equations are provided in this section. Notice that all these equations are eventually based on 4 main transport variables: density, velocity, pressure and temperature (ρ, v, p, T). They are therefore regarded as the solutions of the simulation.

2.1.1 Mass transport modelling

The mass transport equation or as commonly referred to as the continuity equation is presented in equation (2.1). The mass is modelled in the form of density (ρ) or mass per unit volume. The second term in the equation represents the convection of mass into or out of the system with the continuum velocity (v).

$$\frac{\partial \rho}{\partial t} + \nabla \cdot (\rho v) = 0 \tag{2.1}$$

2.1.2 Momentum transport modelling

The momentum transport includes the modelling of linear and angular momentum. The linear momentum is governed by the Navier-Stokes (NVS) equation.

$$\frac{\partial (\rho v)}{\partial t} + \nabla \cdot (\rho v \otimes v) = -\nabla \cdot (p\mathbf{I}) + \nabla \cdot \tau + F_b \tag{2.2}$$

The equation indicates the change of velocity over time due to convection, pressure gradient (∇p), diffusion and body force per unit volume (F_b) acting on the continuum respectively. The pressure gradient term and the diffusion term are regarded as normal and viscous stress tensor. Collectively, they constitute to the stress tensor (σ).

$$\sigma = -(p\mathbf{I}) + \tau \tag{2.3}$$

The conservation of angular momentum is then indicated by the symmetry of this stress tensor.

$$\sigma = \sigma^T \tag{2.4}$$

For Newtonian fluid such as air and water, τ is linearly related to the velocity field through a constant dynamic viscosity (μ) as shown in equation (2.5), where **S** is the strain rate tensor defined by the velocity gradients in equation (2.6).

$$\tau = 2\mu\mathbf{S} - \frac{2}{3}\mu(\nabla \cdot v)\mathbf{I} \tag{2.5}$$

$$\mathbf{S} = \frac{1}{2}(\nabla v + (\nabla v)^{\mathbf{T}}) \tag{2.6}$$

When including gravity (g) in the simulation, the body force term due to gravitational force is modelled as $F_b = \rho g$. The working pressure also becomes piezometric pressure (p_{piezo}) that account for the variation of pressure with the change of altitude (x) as shown in equation (2.7). Note that p_{static} is the static pressure at reference altitude (x_0).

$$p_{piezo} = p_{static} - \rho g \cdot (x - x_0) \tag{2.7}$$

2.1.3 Energy transport modelling

Finally, the thermodynamics in the domain is modelled with the energy transport equation. E denotes the total energy per unit mass and equation (2.8) indicates how it varies over time due to the convection, heat flux ($\dot{q}$), work due to viscous force and work due to body force respectively.

$$\frac{\partial(\rho E)}{\partial t} + \nabla \cdot ((\rho E + p)v) = -\nabla \cdot \dot{q} + \nabla \cdot (\tau \cdot v) + F_b \cdot v \tag{2.8}$$

The energy and pressure (pressure-volume work per unit mass) in the second term then constitute to the enthalpy (H) in the system. Their relationship is illustrated in equation (2.9). The enthalpy can then be defined in term of static enthalpy (H_{static}) and kinetic energy ($\frac{|v|^2}{2}$).

$$\rho E = \rho H - p = \rho(H_{static} + \frac{|v|^2}{2}) - p \tag{2.9}$$

For ideal gas, H_{static} is defined with the specific heat capacity (c_p) and temperature.

$$H_{static} = c_p T \tag{2.10}$$

Now, for fluid domain, all 3 transport equations above are solved. But for fixed solid body, only the energy transport is involved since there are no mass or momentum transfer in the region. Since the velocity is zero, the total energy equals enthalpy and equation (2.8) reduces to:

$$\frac{\partial(\rho c_p T)}{\partial t} = -\nabla \cdot \dot{q} \tag{2.11}$$

The heat flux vector ($\dot{q}$) in equations above comprises of both conductive and convective heat transfer which can be modelled with Fourier's law and Newton's law of cooling respectively.

$$\dot{q} = -\lambda \nabla T + h(T - T_{\infty}) \tag{2.12}$$

where λ is the material thermal conductivity, h is the local heat transfer coefficient and T_{∞} is the characteristic temperature of the surrounding.

For solid, the heat transfer is mainly governed by the conduction, while for air flow, thermal conductivity is low and the heat transfer is governed by the convection. The convection can be categorized into natural convection and forced convection based on the air flow rate. Natural convection occurs when the air flow is low and thus air movement due to buoyancy force can have distinct effect on the rate of heat transfer. Gravity should then be included in the simulation to model this buoyancy effect.

However, for higher air flow rate such as in the case where air is pumped, forced convection applies as the rate of heat transfer from air convection is high and the buoyancy effect can be neglected. The convective term in equation (2.12) should therefore be enough to model the heat transfer. To determine if the buoyancy effect is significant or not, Richardson number (Ri) can be used.

$$\mathrm{Ri} = \frac{g\beta(T - T_{\infty})L}{v^2} \tag{2.13}$$

where β is the thermal expansion coefficient and L is the characteristic length.

For this defroster performance simulation, Ri is estimated to be between 0.1 and 10 according to available boundary conditions. This suggests that both types of convection could be influential and the effect of gravity should be verified in the simulation.

2.2 Fluid film model

The ice layer on the windscreen is an extremely thin sheet with less than 1 mm thickness. Consequently, the fluid film model is used to model this ice layer. Fluid film model simplifies the modelling of thin film by assuming that the film layer is extremely thin and so it can be modelled as a virtual 2-dimensional sheet instead of a physical 3-dimensional volume, eliminating the need of refined mesh in the region.

Fluid film can be used to model both solid and fluid material. It can also be used to model the melting and solidification of fluid as well. The phase of the fluid is determined in term of the solid volume fraction (α_s) which specifies the volume portion of the film that is solid and is calculated as a function of normalized temperature (T^*), where T_L and T_S are the material liquidus and solidus temperature respectively.

$$\alpha_s = \begin{cases} 1 & ; T^* < 0 \\ f(T^*) & ; 0 < T^* < 1 \\ 0 & ; T^* > 1 \end{cases} \tag{2.14}$$

$$T^* = \frac{T - T_S}{T_L - T_S} \tag{2.15}$$

In case for equal T_L and T_S, the denominator in equation (2.15) is set to 0.002 K automatically. $f(T^*)$ is the fraction solid curve determining the phase change function. For linear melting assumed, it is defined as

$$f(T^*) = 1 - T^* \tag{2.16}$$

To model the melting and solidification of material in the fluid film, the energy transfer due to phase change is accounted in the energy transport equation with an additional latent enthalpy of fusion (H_{fus}) as a function of the solid volume fraction. The enthalpy term in film energy transport equation becomes

$$H_{film} = H + (1 - \alpha_s) H_{fus} \tag{2.17}$$

Now, all transport equations still hold for fluid film but they are solved for only 2 dimensions and an additional film thickness variable ($\mathbb{h}_{film}$) is included to model the virtual film thickness ($\mathbb{h}_{film}$) by multiplying to the equations. The film thickness is solved in the continuity equation which becomes

$$\frac{\partial \rho \mathbb{h}_{film}}{\partial t} + \nabla \cdot \left(\rho v \mathbb{h}_{film} \right) = S_m \tag{2.18}$$

Note that if there is a mass source/sink phenomenon included, for instance from droplets impingement, splashing, film stripping, evaporation or condensation, it can be included as mass source per unit film area term (S_m). The effect on the momentum and energy from these phenomena is then included in the momentum and energy transport equation as the source term per unit film area as well. Nevertheless, since these phenomena are not related to the defroster performance or at least not in the area of interest, their detailed modelling are not included in this review. The film thickness is set as initial condition in the simulation instead.

For the momentum transport equation, the flow is assumed to be laminar in fluid film due to thin boundary layer flow. A parabolic velocity profile is then assumed in the direction normal to the wall since the velocity is solved in only 2 dimensions. The normal components of the viscous and convective term are also assumed negligible.

Note that for fluid film, surface tension could play an important role in determining the flow distribution through the capillary and thermo-capillary convection. The capillary effect can influence the size and shape of water droplets forming on the windscreen. It also leads to the partial wetting phenomenon as the water flows down in non-continuous film as well. The thermo-capillary convection effect then occurs when there is a gradient of the surface tension due to different concentration or temperature of fluids. The gradient of the surface tension can induce a convective motion and thus affecting the flow pattern as well. These phenomena can be accounted as an additional capillary pressure, partial-wetting stress tensor and thermo-capillary stress tensor term in the momentum and energy transport equation.

In this study, partial wetting is present when the ice is melted and the water droplets form and flow down the windscreen. The temperature change can also induce the thermo-capillary stress. However, the focus of this study is on the melting pattern of the ice rather than the flow pattern of the water after melt. Although the water droplets' trail can also affect the melting pattern, it should not be up to a significant extent since the melting occurs from the bottom and then proceeds upward. Therefore, the simulation is simplified by keeping the ice viscosity in the film for the whole simulation and completely ignore the water flow. The water film is then fixed on the windscreen whether gravity is included or not. This also allows larger time step size to be used in the simulation since the fluid motion with small timescale is neglected.

Certainly, the presence of water film on the windscreen after the ice has melted could affect the heat transfer and the temperature profile after melt might not be as accurate. This will be a part of the evaluation in this study as well.

2.3 RANS turbulence models

Turbulence is a phenomenon denoting irregularity in the flow pattern arising from instabilities at high flow rate. For the fluid of such low kinematic viscosity as air, it is most likely that the flow is turbulent even with low velocity. Since turbulence is another factor that can affect the transport of mass, momentum and energy as well, it needs to be accounted for in order to simulate the flow correctly.

Turbulence complicates the flow field as it induces small scale/high frequency irregular fluctuation of the transport quantities called stochastic behavior. This means it would be expensive to solve the flow directly in such small scale since large computational resource will be required. To avoid this, turbulence is simulated with turbulence models based on its physics instead. The most popular and cheapest model is called **Reynolds-Averaged Navier-Stokes (RANS) model**, in which the averaged transport quantities are solved for instead of the stochastic instantaneous quantities and then additional models are used to provide closure for the averaged equations. This effectively removes the computationally expensive fluctuation while still offers robust modelling for most flows and thus, RANS model becomes more suitable for industry use and the selected choice in this study.

In RANS model, the instantaneous transport variables (ϕ) in the governing transport equations are decomposed into mean and fluctuating components ($\bar{\phi}, \phi'$) as shown in equation (2.19). This is called **Reynolds decomposition**.

$$\phi = \bar{\phi} + \phi' \tag{2.19}$$

Then, to discard the fluctuating components from the equations, the transport equations are averaged (time-averaging for steady state simulation and ensemble averaging for transient simulation). This results in the same transport equations but with mean quantities ($\bar{v}, \bar{p}, \bar{E}, \bar{q}, \bar{\tau}$) and an additional Reynolds stress tensor term (τ_{RANS}) in momentum and energy equation as the term $\nabla \cdot \tau$ becomes $\nabla \cdot (\bar{\tau} + \tau_{RANS})$. The additional τ_{RANS} term originates from the nonlinear interaction between the fluctuating velocity components where k denotes the turbulence kinetic energy.

$$\tau_{RANS} = -\rho \begin{pmatrix} \overline{v_i' v_i'} & \overline{v_i' v_j'} & \overline{v_i' v_k'} \\ \overline{v_j' v_i'} & \overline{v_j' v_j'} & \overline{v_j' v_k'} \\ \overline{v_k' v_i'} & \overline{v_k' v_j'} & \overline{v_k' v_k'} \end{pmatrix} + \frac{2}{3}\rho k \mathbf{I} \tag{2.20}$$

This τ_{RANS} term requires additional modelling for the equations to be closed. One alternative is called **the Eddy viscosity model** in which, the momentum transfer from turbulent motion is assumed to be diffusive and the τ_{RANS} term can be modelled with the turbulent viscosity or eddy viscosity (μ_t) in analogous to the dynamic viscosity for molecular gradient-diffusion. Based on **Boussinesq approximation**, the τ_{RANS} term is assumed to be linearly proportional to the mean strain rate tensor ($\bar{\mathbf{S}}$) and μ_t. These are similar to the modelling of the viscous stress tensor τ in equation (2.5) and (2.6).

$$\tau_{RANS} = 2\mu_t \bar{\mathbf{S}} - \frac{2}{3}(\mu_t \nabla \cdot \bar{v})\mathbf{I} \tag{2.21}$$

$$\bar{\mathbf{S}} = \frac{1}{2}(\nabla \bar{v} + \nabla \bar{v}^{\mathbf{T}}) \tag{2.22}$$

With this concept, μ_t term needs further modelling as it becomes the new unknown. Akin to how molecular dynamic viscosity is related to velocity and length scale, μ_t can be modelled as a function of 2 additional scalar turbulence transport quantities which can be used to determine the turbulent velocity and length scale. Since only 2 additional transport equations are needed to solve for these 2 terms, this eddy viscosity model is less expensive than the alternative Reynolds stress transport model (RST) in which additional transport equations are solved for each component in the τ_{RANS} term directly. Thus, it is a common choice for industry applications and so it is selected in this study. Several choices of Two-equation models are available including different modifications of k-epsilon (KE) and k-omega (KO) models. Realizable KE, LEB KE and SST KO models are chosen in this study and are described in the next subsections. The wall treatment applied in the simulation is also presented as well.

2.3.1 Realizable k-epsilon model

k-epsilon model (KE) is one of the most robust and thus most commonly used turbulence models in the industry. It has acceptable accuracy and stability for most types of flow and even with complex recirculation. There are several modifications of the KE models since the model has been studied and improved for decades. In standard k-epsilon (SKE) model [1, 2], according to equation (2.20) and (2.21), there is a possibility that the $\overline{v_i' v_j'}$ term can become unphysically negative in flow with high strain rate. The Realizable k-epsilon (RKE) model [3] is modified to solve this problem with revised ε transport equation and model coefficient C_μ. This should generally give better or at least as accurate result compared to that of SKE. Thus, RKE model is selected in this study.

Governing equations

In RKE model, turbulent eddy viscosity is modelled as a function of turbulent kinetic energy (k) and turbulent dissipation rate (ε), where t_t indicates the turbulence time scale and is equal to large eddy time scale t_{te} in this case.

$$\mu_t = \rho k C_\mu f_\mu t_t \tag{2.23}$$

$$t_t = t_{te} = \frac{k}{\varepsilon} \tag{2.24}$$

Note that from here onwards, C will denote model coefficient and f will denote model function which are defined in the Appendix. In this case, C_μ is modified from a constant in SKE to be a function of mean flow and turbulent properties in RKE with a damping function f_μ.

2 transport equations are then solved for k and ε. The terms in the equations below expresses the accumulation, convection by mean velocity, molecular diffusion, turbulent diffusion, production and dissipation of the transport variables respectively. f_2 is a damping factor as a function of k and ε.

$$\frac{\partial(\rho k)}{\partial t} + \nabla \cdot (\rho \bar{v} k) = \nabla \cdot \left[\left(\mu + \frac{\mu_t}{C_{\sigma k}} \right) \nabla k \right] + (P_k - \Upsilon_M) - \rho \varepsilon \tag{2.25}$$

$$\frac{\partial(\rho \varepsilon)}{\partial t} + \nabla \cdot (\rho \bar{v} \varepsilon) = \nabla \cdot \left[\left(\mu + \frac{\mu_t}{C_{\sigma \varepsilon}} \right) \nabla \varepsilon \right] + \frac{1}{t_{te}} C_{\varepsilon 1} P_\varepsilon - C_{\varepsilon 2} f_2 \rho \left(\frac{\varepsilon}{t_{te}} \right) \tag{2.26}$$

The production term P_k for k includes the production due to mean velocity gradient (G_k) and buoyancy (G_b) if gravity is included, while the Υ_M term accounts for the compressibility effect in the k production [4]. The production term P_ε for ε includes the dissipation by strain rate and the buoyancy. Note that, as a modification from SKE, G_k is removed from P_ε term in RKE to avoid singularity in the destruction term and thus RKE offers better prediction of the turbulence dissipation rate.

$$P_k = G_k + G_b \tag{2.27}$$

$$P_\varepsilon = |\bar{\mathbf{S}}|k + C_{\varepsilon 3}G_b \tag{2.28}$$

$$G_k = \mu_t|\bar{\mathbf{S}}|^2 - \frac{2}{3}\rho k\nabla\cdot\bar{v} - \frac{2}{3}\mu_t(\nabla\cdot\bar{v})^2 \tag{2.29}$$

$$G_b = \frac{\beta\mu_t}{\mathrm{Pr_t}}\nabla\bar{T}\cdot\mathrm{g} \tag{2.30}$$

$$\Upsilon_M = \frac{\rho C_M k\varepsilon}{v_c^2} \tag{2.31}$$

where $\mathrm{Pr_t}$, $\mathbf{g}$, v_c denotes the turbulent Prandtl number, gravitational vector and speed of sound respectively. For ideal gas, $\beta = -\frac{1}{\rho}\frac{\partial\rho}{\partial\bar{T}}$ and for air, $\mathrm{Pr_t} = 0.9$.

Note that KE model has limited performance in the low turbulence region where both k and ε approach zero since the dissipation terms for both quantities are mutually dependent on each other. The KE model is consequently modified with **Two-layer approach** [5] to deal with the near-wall modelling so the transport equations can be solved up until the wall in the viscous affected layer. The Two-layer approach divides the domain into bulk and near-wall layer. The near-wall turbulent viscosity is modelled with an algebraic correlation based on wall distance Reynolds number (Re_d) instead [6] and then it is blended with the μ_t in the bulk using the wall-proximity indicator function f_λ.

$$\mu_t = f_\lambda\mu_{t-bulk} + (1-f_\lambda)\mu_{t-near-wall} \tag{2.32}$$

$$\mu_{t-near-wall} = 0.42\mu Re_d C_\mu^{1/4}\left[1-\exp\left(-\frac{Re_d}{70}\right)\right] \tag{2.33}$$

$$Re_d = \frac{\rho\sqrt{k}y}{\mu} \tag{2.34}$$

where y denotes the distance to the nearest no slip wall.

Since Re_d is based on k, k needs to be solved for the whole domain. Nevertheless, due to the problem with solving ε next to the wall, an imposed value of the near-wall ε is used in the k transport equation when solving in the near-wall region. $\varepsilon_{near-wall}$ is calculated from an algebraic equation which is a function of k and length scale (l_ε) [6].

$$\varepsilon_{near-wall} = \frac{k^{\frac{3}{2}}}{l_\varepsilon} \tag{2.35}$$

$$l_\varepsilon = C_l y\left[1-\exp\left(-\frac{Re_d}{2C_l}\right)\right] \tag{2.36}$$

2.3.2 LEB k-epsilon model

Lag elliptic blending k-epsilon (LEB KE) [7, 8] is another modification of KE model which improves the modelling of turbulence anisotropy and reduces the model dependency on the Reynolds number in KE model. Major adaptations include the modified definition of ε, 2 new turbulence transport variables and additional terms to account for increase near-wall dissipation rate and the redistribution of wall-normal velocity fluctuations[9]. Furthermore, the stress-strain lag concept is also incorporated in one of the additional production terms to avoid the over-prediction of k [10]. As a result, LEB KE model yields better performance in low Reynolds number flow, flow with separation, near-wall flow and near-wall heat transfer compared to SKE and RKE model, while also remains more stable compared to KO model as well. Thus, it is one of the selected choices in this study.

Governing equations

In LEB KE model, the turbulent viscosity is modelled with modified $C_{\mu LEB}$, C_{tLEB} and t_{tLEB} from RKE model as denoted by the subscript LEB. The model is based on an additional non-dimensional variable called the normalized wall-normal stress component φ which represents the ratio between the wall-normal Reynolds stress to k and thereby accounts for the turbulence anisotropy near the wall.

$$\mu_t = \rho k C_{\mu LEB} \varphi \left[min\left(t_{tLEB}, \frac{1}{\sqrt{3} C_{\mu LEB} \varphi |\bar{\mathbf{S}}|} \right) \right] \tag{2.37}$$

$$t_{tLeb} = \sqrt{t_{te}^2 + C_{tLEB}^2 \frac{\nu}{\varepsilon}} \tag{2.38}$$

where ν denotes the kinematic viscosity.

Hence, in addition to k and ε, another transport equation is solved for φ. Moreover, a non-dimensional blending factor α is introduced in the production terms of ε and φ to merge the near-wall effect into the model. An additional elliptic equation is then used to solve for this blending factor. Note that ε definition in this model is modified to homogeneous ε instead since it is less affected by the Reynolds number. This results in the molecular diffusion term in all the transport equations reduced by half.

$$\frac{\partial(\rho k)}{\partial t} + \nabla \cdot (\rho \bar{v} k) = \nabla \cdot \left[\left(\frac{\mu}{2} + \frac{\mu_t}{C_{\sigma k}} \right) \nabla k \right] + (P_k - \Upsilon_M) - \rho(\varepsilon) \tag{2.39}$$

$$\frac{\partial(\rho \varepsilon)}{\partial t} + \nabla \cdot (\rho \bar{v} \varepsilon) = \nabla \cdot \left[\left(\frac{\mu}{2} + \frac{\mu_t}{C_{\sigma \varepsilon}} \right) \nabla \varepsilon \right] + \frac{C_{\varepsilon 1 Leb}}{t_{te}} P_{\varepsilon LEB} - C_{\varepsilon 2} \rho \left(\frac{\varepsilon}{t_{te}} \right) \tag{2.40}$$

$$\frac{\partial(\rho \varphi)}{\partial t} + \nabla \cdot (\rho \bar{v} \varphi) = \nabla \cdot \left[\left(\frac{\mu}{2} + \frac{\mu_t}{C_{\sigma \varphi}} \right) \nabla \varphi \right] + P_{\varphi} \tag{2.41}$$

$$\nabla \cdot (l_t^2 \nabla \alpha) = \alpha - 1 \tag{2.42}$$

where l_t is the turbulent length scale defined by:

$$l_t = C_L \sqrt{\frac{k^3}{\varepsilon^3} + C_\eta^2 \sqrt{\frac{\nu^3}{\varepsilon}}} \tag{2.43}$$

The production term P_ε in RKE is modified to $P_{\varepsilon Leb}$ with G_k term as in SKE and an additional term G_a accounting for the increase of near-wall dissipation rate. For φ, the production term P_φ depends on the turbulent and buoyancy production term (G_k, G_b) and model function f_W and f_h. f_W and f_h account for the redistribution of wall-normal velocity fluctuations at the wall and homogeneous zone due to pressure fluctuations from the wall, thereby improve the near-wall turbulence anisotropy and the kinematic blocking of the wall modelling. The stress-strain lag concept is also incorporated in the f_h term to reduce the over-prediction of k in non-equilibrium flow usually occurred in SKE model due to the misalignment of the principal components in the stress and strain rate tensor [10]. Finally, the blending factor α allows the effect from the G_a and f_W to be present near the wall and disappear in the far-field, and vice-versa for the f_h. Thus, blending the KE modelling for high Re flow at bulk with the LEB near-wall modelling with φ and α.

$$P_{\varepsilon LEB} = G_k + C_{\varepsilon 2} G_b + \frac{1}{C_{\varepsilon 1\mathrm{LEB}}} G_a \tag{2.44}$$

$$G_a = C_k (1-\alpha)^3 \nu \mu_t \frac{k}{\varepsilon} [\nabla \cdot (|2\bar{\mathbf{S}}\mathbf{n}|\mathbf{n})]^2 \tag{2.45}$$

$$P_\varphi = -(2 - C_{\varepsilon 1\mathrm{LEB}}) \frac{\varphi}{k} (G_k + G_b) + \rho(1-\alpha^3) f_W + \rho \alpha^3 f_h \tag{2.46}$$

where **n** indicates the wall normal direction.

2.3.3 SST k-omega model

k-omega (KO) turbulence model [11, 12] is another popular model used in the industry. In contrast to KE, KO model eliminates the problem with modelling ε in the near-wall region with the use of specific dissipation rate ω instead of ε, allowing the model to be applicable in all zones up to the near-wall boundary layer without the need for special wall functions. KO model thus has better accuracy for boundary layer zone with adverse pressure gradient and is mostly used for the aerospace application.

However, in contrast to KE model, KO model is more sensitive to ω value in the free-stream and inlet boundary condition. A modification of the standard k-omega model called SST KO model is then proposed to solve this problem by using a revised transport equation of ω and incorporating the use of the more stable KE model in the bulk region with the help of the cross-diffusion term and the blending function [13]. With presumably better modelling of the near-wall flow, SST KO model is selected as an alternative in this study as well.

Governing equations

In SST KO, the turbulent viscosity is modelled with k and ω. ω is defined as the dissipation rate per unit turbulent kinetic energy $\omega \propto \frac{\varepsilon}{k}$ and is seen as an inverse of the dissipation time scale.

The turbulent time scale is modified to t_{tKO} and is calculated with Durbin's realizability constraint [14]. Blending function F_2 is used to account for the wall distance (y). The use of mean strain rate tensor instead of mean vorticity tensor then has extended its application beyond aerospace application.

$$\mu_t = \rho k t_{tKO} \tag{2.47}$$

$$t_{tko} = \min\left(\frac{1}{\omega}, \frac{C_{a1}}{|\bar{\mathbf{W}}|F_2}\right) \tag{2.48}$$

$$F_2 = \tanh\left(\left(\max\left(\frac{2\sqrt{k}}{C_{\beta^*}\,\omega y}, \frac{500\nu}{y^2\omega}\right)\right)^2\right) \tag{2.49}$$

2 transport equations are solved for k and ω. In SST KO, the ω transport equation in transformed from ε transport equation in SKE model. Notice that the dissipation term of ω is independent of k and so the problem with the near-wall zone modelling occurred in KE model is avoided.

$$\frac{\partial(\rho k)}{\partial t} + \nabla\cdot(\rho\bar{v}k) = \nabla\cdot[(\mu + C_{\sigma kko}\mu_t)\nabla k] + P_k - \rho C_{\beta^*}(\omega k) \tag{2.50}$$

$$\frac{\partial(\rho\omega)}{\partial t} + \nabla\cdot(\rho\bar{v}\omega) = \nabla\cdot[(\mu + C_{\sigma\omega}\mu_t)\nabla\omega] + P_\omega - \rho C_{\beta KO}\omega^2 \tag{2.51}$$

Now, instead of including the compressibility modification Υ_M in the P_k production term, the compressibility is accounted for by including the compressibility factor as a function of turbulent Mach number M_t in the coefficient C_{β^*} and $C_{\beta ko}$ instead [15], see Appendix. Turbulent Mach number is defined as

$$M_t^2 = \frac{2k}{v_c^2} \tag{2.52}$$

For ω, the production term P_ω includes specific dissipation production (G_ω) and cross diffusion term ($G_{\omega D}$). G_ω is a function of the turbulent production term G_k, while the $G_{\omega D}$ term is based on the dot production $\nabla k\cdot\nabla\omega$.

$$P_\omega = G_\omega + G_{\omega D} \tag{2.53}$$

$$G_\omega = \rho C_\gamma\left[\left(|\bar{\mathbf{S}}|^2 - \frac{2}{3}(\nabla\cdot\bar{v})^2\right) - \frac{2}{3}\omega\nabla\cdot\bar{v}\right] \tag{2.54}$$

$$G_{\omega D} = 2\rho(1-F_1)C_{\sigma\omega 2}\frac{1}{\omega}\nabla k\cdot\nabla\omega \tag{2.55}$$

SST KO model incorporates both KE and KO model in the simulation by the use of the blending function F_1 in $G_{\omega D}$ and other model coefficients. The blending function is a function of wall distance, turbulent transport quantities and the cross-diffusion coefficient. In the area close to the wall, the blending function reduces the impact from $G_{\omega D}$ term in ω production and the model is similar to standard KO. As the zone gets farther from the wall, the blending function then increasingly includes $G_{\omega D}$ in the ω production, leading to simulation result identical to that of the KE model. The blending function hence blends results from KO model in the near-wall region with the results from KE model in the bulk region effectively.

2.3.4 Turbulence wall treatment

As discussed in previous sections, the modelling in the near wall region could be challenging due to different conditions in the boundary layer compared to the bulk region. In this study, the main flow of interest from the defroster impinges on the internal side of the windscreen where the heat is then transferred to the ice layer on the external side. Thus, the modelling near the wall could be influential to the result and worth reviewing.

The near-wall modelling can be categorized into 2 aspects, the near-wall modelling in the turbulence models and the wall treatment. The first aspect is the wall effect accounted in the turbulence model itself and has been partially discussed in previous sections such as the Two-layer approach in KE model and the blending function in KO model. With these near-wall modelling adaptations, the turbulence models work well near the wall and do not require special wall treatment anymore. However, with these approaches, refined mesh and thus large computational resource are still required to resolve the flow in the viscous sub-region without the wall treatment. Consequently, the wall treatment is still applied to increase the efficiency of the simulation.

The wall treatment is used to provide wall boundary conditions for the flow, energy and turbulence for solution next to the wall. This is done by calculating turbulent transported quantities values to be imposed in the near-wall cell centroids using the wall function. In addition, wall shear stress (τ_w) and wall heat flux ($\dot{q}_w$) are calculated to be used in the momentum and energy transport equations as well.

The wall function approximates the turbulent transported quantities by the use of non-dimensional quantities that are independent of the flow characteristic (Reynolds number) and are defined based on the physics in either the viscous sub-layer or log layer in the wall boundary layer. Thus, standard wall function usually works well when the thickness of the near wall cell falls within the range of these layers and might not be as accurate if it lies within the range of the buffer layer. An adapted wall function called **the blended wall functions** is therefore selected in this study instead. This blended wall function merges the functions for the viscous sublayer and the log layer together and so it is applicable for all boundary layers and a wide range of near-wall cell thickness can be used.

Blended wall function

For KE and KO model, the turbulent transport quantities include k, ε and ω. For k, the transport equation is solved with imposed value of P_k and ε in the near-wall cell. For ε and ω, imposed values are calculated without solving their transport equations.

The calculation of imposed quantities (P_k, ε and ω) is done by equating the definition of the non-dimensional turbulent quantities (P_k^+, ε^+, ω^+) with their algebraic approximation from the wall function. The rearranged definitions below show the imposed quantities as a function of non-dimensional quantities which is calculated by the wall function in the right hand-side. Note that the non-dimensional quantities (P_k^+, $\omega^+$and $\hat{T}_C^+$) are given by the blended wall function which includes the component for the viscous-sublayer and log layer respectively, while ε^+ formulation is modified to follow the Two-layer model instead. f_γ is a blending function as a function of Re_d that is used to blend these components together.

Rearranged non-dimensional definition	**Wall function approximation of non-dimensional quantities**	
$P_k = \frac{\rho^2 u^{*4} P_k^+}{\mu}$	$P_k^+ = f_\gamma \left(\mu_t^+ \frac{\partial u^+}{\partial y^+}\right) + \left(1 - f_\gamma\right) \frac{1}{C_\kappa y^+}$	(2.56)
$\varepsilon = \frac{\rho u^{*4} \varepsilon^+}{\mu}$	$\varepsilon^+ = \frac{\left(k^+\right)^{3/2}}{y^+ l_\varepsilon^+}$	(2.57)
$\omega = \frac{\rho u^{*2} \omega^+}{\mu}$	$\omega^+ = f_\gamma \frac{6}{C_\beta (y^+)^2} + \left(1 - f_\gamma\right) \frac{1}{\sqrt{C_{\beta^*}} C_\kappa y^+}$	(2.58)

Other non-dimensional quantities appeared above are defined as

$$\left.\begin{aligned} y^+ &= \frac{y \rho u^*}{\mu} & l_\varepsilon^+ &= \frac{l_\varepsilon}{y} \\ \mu_t^+ &= \frac{\mu_t}{\mu} & k^+ &= \frac{k}{u^{*2}} \end{aligned}\right\} \quad (2.59)$$

u^+ is defined as $u^+ = \frac{v_{\parallel w}}{u^*}$, with $v_{\parallel w}$denoting the wall tangential velocity. Yet, in the simulation, it is found through Reichhardt's law [16].

$$u^+ = \frac{1}{C_\kappa} \ln(1 + C_\kappa y^+) + C_w \left(1 - e^{-\frac{y^+}{C_{ym}}} - \frac{y^+}{C_{ym}} e^{-C_b y^+}\right) \quad (2.60)$$

The characteristic velocity scale near the wall or the wall friction velocity (u^*) is also given by the blended wall function with components from both viscous sublayer and log layer.

$$u^* = f_\gamma \left(\frac{\mu |v_{\parallel w}|}{\rho y}\right)^{1/2} + \left(1 - f_\gamma\right)\left(C_\mu^{1/4} k^{1/2}\right) \quad (2.61)$$

Wall shear stress calculation

For laminar flow as in the fluid film, wall shear stress follows the Newtonian fluid stress tensor calculation in equation (2.5) with the use of tangential velocity gradient at the wall instead. However, for turbulent flow, wall shear stress (τ_w) needs to account of the increasing shear stress from the turbulent mixing in the boundary layer as well. It is defined as the magnitude of wall shear force (τ_{wf}) in the direction tangential to the wall which is determined as a function of u^*.

$$\tau_w = |\tau_{wf}| = \left|\rho u^{*2} \frac{\hat{\mathrm{v}}_{\parallel w}}{|\hat{\mathrm{v}}_{\parallel w}|}\right| \quad (2.62)$$

Wall heat flux calculation

Finally, for laminar flow as in the fluid film, the wall heat flux is simply calculated from the wall conduction heat flux term in equation (2.12). For turbulent flow, the wall heat flux is instead modelled as the convection of enthalpy as a function of u^* and the difference between the RANS averaged near-wall cell temperature ($\hat{T}_C$) and wall temperature (T_w) normalized by the non-dimensional near-wall cell temperature ($\hat{T}_C^+$). $\hat{T}_C^+$ is given by the wall function as a function of y^+ and Prandtl number (Pr) that indicates the ratio between heat conductivity to the diffusion.

$$\dot{q}_w = \rho c_p u^* \frac{\hat{T}_C - T_w}{\hat{T}_C^+} \tag{2.63}$$

$$\hat{T}_C^+ = \exp(-C_\Gamma)\,\mathrm{Pr}\,y^+ + \exp\left(-\frac{1}{C_\Gamma}\right)\mathrm{Pr_t}\left[\frac{1}{C_\kappa}\ln(C_E y^+) + C_{Pr}\right] \tag{2.64}$$

$$\mathrm{Pr} = \frac{c_\mathrm{p}\mu}{\lambda} \tag{2.65}$$

3 Methodology

This chapter presents the working process of this thesis along with the necessary setup in each stage. The chapter first describes the general procedure of the defroster performance testing implemented at Volvo Cars and the types of test data available for the simulation result validation. Then, the default CFD simulation setup including the pre-processing and post-processing steps used in this study is defined. After the mesh independence study to identify the optimal mesh size, the choices of solvers and models are verified in the model verification section. The boundary conditions and geometry are then verified in subsequent sections in order to improve the accuracy of the results. Finally, after the most desirable simulation scheme is established, it is implemented on another car model in order to assess its reliability for further industry application.

3.1 Defroster performance testing procedure

EU 672/2010 regulation specifies the requirements for the defroster system in term of the clear vision criteria in certain vision areas after a period of testing time as listed in Table 3.1. The vision areas are indicated in the regulation as illustrated in Figure 3.1 and thus they become the area of interest in this study.

Table 3.1 Clear vision requirement according to EU672/2010 regulation.

Testing time [minutes]	Area A		Area B
	Driver side	Passenger side	
20	≥ 80%		
25		≥ 80%	
40			≥ 95%

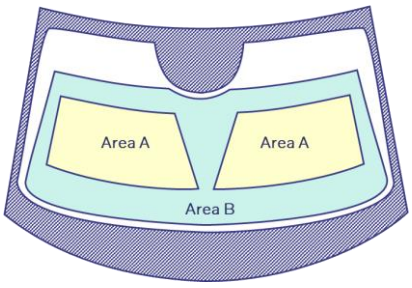

Figure 3.1 Vision area on the windscreen according to EU672/2010 regulation.

At Volvo Cars, defroster performance testing is carried out in a closed chamber with controllable air flow rate and temperature set to follow the testing conditions defined in the EU regulation. The air flow directed towards the front windscreen is evenly distributed through the grated screen situated about 1 – 2 m in front of the car. For the whole test duration, the air flow shall be maintained at the rate as low as possible and not exceeding 8 km/h (2.22 m/s). In this case, the air flow is maintained at 0.78 m/s.

The preparation for the test begins with leaving the complete vehicle with engine switched off in a -18 ± 3 ℃ environment overnight for at least 10 hours. After that, a spray gun is used to spray water over the windscreen and all windows. The amount of water is calculated so that it can form an even layer of 0.044 g of ice per 1 cm^2 windscreen area. In this case, 0.046*1.1 cm^3 of water is used per 1 cm^2 windscreen

area. The addition 10% from the requirement is supposed to account for any possible spill. After 30 – 40 minutes of waiting time for the ice layer to develop, the engine is switched on and the test can then begin. The engine is maintained at 1500 rpm for the whole test duration and ‘Max defroster mode’ is implemented in the test. The test is usually carried out for 40 minutes or until the ice sheet is completely melted.

Regarding result monitoring, temperature probes are installed at various locations to record the temperature profile during the test. Typically, the probes are placed at the inlets and outlets of the HVAC, at each defroster vent outlets and outside the car. The defrosted area is then outlined from the inside of the windscreen at 5-minute interval and the contour plot of these outlines is recorded at the completion of the test to use as proof that the vehicle model passes the regulation. The typical test data thus includes the temperature profiles and the contour plot of the ice melting pattern.

Nevertheless, to validate simulation result, more detailed test data is desirable. A special test was therefore performed for this purpose. The test was done in March 2019 prior to the beginning of this thesis and thus, it set out conditions for this study. In this test, Volvo VA model was used as the test subject and the test was performed according to typical performance testing procedure. However, additional temperature probes were installed on the internal and external side of the windscreen and front side windows (will be regarding as Ext and Int probe respectively in this report) as well as under the IP panel to better observe the phenomena in these areas. The location of the temperature probes set on the front windscreen and their probe number are shown in Figure 3.2. Moreover, in addition to the ice melting pattern contour plot, a video was recorded at several angles around the car (for front, side and rear windscreens) for the whole test interval for better investigation.

With these additional data, the simulation result could be better validated. Thus, the geometry and boundary conditions in the simulations are set based on this test condition. The temperature profiles from the Ext and Int probes as well as the visualization of the ice melting pattern on the windscreen and front side windows are compared to these test data for validation.

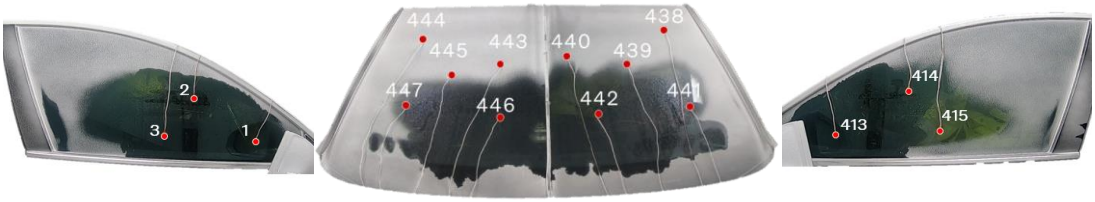

Figure 3.2 Temperature probe locations on the windscreen and front side windows in defroster performance test.

For the final simulation scheme validation, data from another test on Volvo VB was selected. This test was done in February 2014 and it only followed the typical testing procedure with an addition of photographic records of the ice melting pattern on the windscreen at 5-minute interval between 10 – 25 minutes testing time. Therefore, only the ice melting pattern was compared in the validation.

3.2 CFD simulation setup

This section describes the simulation setup including the geometry, its pre-processing and different settings for the computational regions, boundary conditions, mesh, physics continua and result monitoring. These settings will be considered as default settings used throughout this study if not specified otherwise.

3.2.1 Geometry

As prescribed by the available test data, the computational domain in this study is generated based on Volvo VA geometry. Concerned geometry parts include the cabin interior, defroster duct system, windscreen and side windows as illustrated in Figure 3.3. The windscreen and windows each consist of 3 layers made of glass, foil, and glass respectively. Note that HVAC unit is not included in this simulation and therefore other air duct system for instance of the center or side vents are not included either.

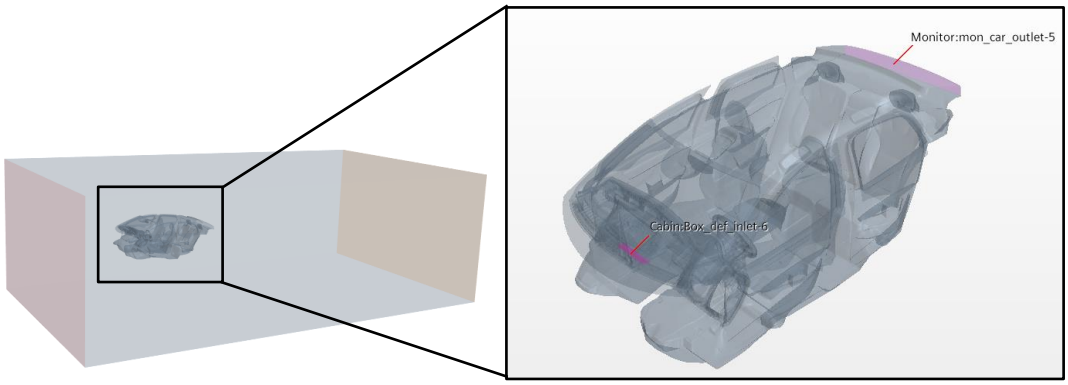

Figure 3.3 Volvo VA computational domain.

Additionally, since the ice sheet situates on the external side of the windscreen and windows and external convection is to be simulated, a block is created to contain the external air domain. The block size is arbitrary. It is built just so it is large enough to avoid its boundary effect on the results. Moreover, the rear section of the car is removed and the area above the rear seats illustrated as 'Monitor: mon_car_outlet-5' in Figure 3.3 serves as a passage connecting the air between the cabin interior and the external air domain. The inlets of the computational domain are at the front side of the block (domain inlet) and at HVAC-defroster connection (defroster inlet). Finally, the rear side of the block acts as the outlet of the computational domain.

3.2.2 Geometry pre-processing

The CAD model of concerned geometry parts is first pre-processed in ANSA pre-processor program (Version 19.0.2). The geometry is cleaned and modified to ensure closed, manifold and non-intersecting surfaces. Monitor surfaces are created at inlets, outlets and at vent outlets so a surface averaged data at these regions can be achieved later in the simulation. After the external domain is built, all the surfaces are meshed and then exported as a Nastran file to be used as an input for the simulation. This surface mesh serves as a simplified representation of the geometry which is more suitable for CFD simulation.

After importing the surface mesh of the geometry into STAR-CCM+ (version 2019.3) where the rest of the simulation are executed, the geometry is further prepared. 3 layers of the windscreen/window are imprinted together to get rid of pierced surfaces and ensure well conformation. A surface wrap is then used to wrap around all parts (excluding the monitor surfaces) to improve the surface quality and create a sealed air domain. This takes less than 1 hour to accomplish. The final computational domain thus consists of the air domain and each layers of the windscreen/window. Note that the rear side windows are not included in the computational domain as they are not the focus of this study. And since the heat conduction is to be simulated only through these windscreen/window layers, no other solid parts are included in the computational domain either.

3.2.3 Region and boundary conditions settings

In STAR-CCM+, computational domains are assigned to 'region' where the physics is to be simulated. Meshing is then executed on these regions. However, before the volume mesh is generated, the boundary conditions shall be set to avoid the generation of prism layers at inlet and outlet surfaces.

For most surfaces, the boundary condition remains the default non-slip wall with adiabatic thermal boundary condition. For inlet surfaces, the boundary conditions are set following the measurements during the performance test. Since the available data are in terms of air flow velocity and volumetric flow rate, **fixed velocity inlet** is selected as the inlet boundary condition. The domain inlet velocity is set to 0.78 m/s with a constant temperature of -16 ℃. For the defroster inlet, the company required a 100 l/s air flow rate, which is about 6 m/s for the area of this inlet. During the test, the temperature at defroster inlet is ramped up over time from -18 to 43 ℃. The average temperature profile from the probes installed at the HVAC-defroster connection available at 1 s interval is thus used as a table input for the defroster inlet temperature in transient simulation. For both inlets, the default turbulent intensity and viscosity of 0.01 and 10 are used respectively. Then, for outlet surface, **pressure outlet** boundary condition is applied with static temperature set to -16 ℃. Now, in addition to boundary conditions, interfaces are also created to support the transfer of simulation data such as energy transfer across regions. In this study, interfaces are created in-between the windscreen/window layers and between these layers and the air domain.

Finally, a shell region is inserted at the interface between the air domain and the external layer of the windscreen/windows. 2 additional interfaces connecting the shell region to the air domain and the windscreen/window layer are then automatically formed. This shell region is a 2-dimensional region with no physical thickness used to simulate the ice layer with the fluid film modelling.

3.2.4 Meshing

In CFD simulation, the transport equations are solved over each discretized volume in the computational region to obtain local transport quantities that describe the flow characteristics in the domain. The collection of these discretized volumes is referred to as mesh which is created by surface and volume meshing of the computational region.

For the air domain, polyhedral mesh is used to better capture the flow features and yield more accurate solutions. Prism layers are also included to allow better resolution in the near-wall region. Parallel meshing is performed in this region to increase the

meshing speed. For the windscreen/window layers, since the geometry is thin and well structured, thin mesher which produces a more organized prismatic cells similar to the prism layers is preferred. But the thin mesher is not compatible with parallel meshing so serial meshing is used for these parts. Note that the proper mesh size will be discussed in the mesh independence study in Section 3.3.

After the mesh is completely generated, the mesh quality is checked and invalid cells are removed from the computational regions to improve the simulation stability and accuracy. The criteria for the invalid cells follow general recommendation from STAR-CCM+ support center listed as followed.

Cells within the following criteria are removed.

- Face validity < 0.999
- Cell quality < 1 e-5
- Volume change < 1 e-10
- Contiguous cell < 1000
- Connected face area < 0 m^2
- Volume < 0 m^3
- Cell warpage quality < 0.3
- Skewness angle > 85

3.2.5 Physics continua settings

Physics continuum is a section containing models, solvers, materials and initial conditions selected to represent the physics of the simulation. Physics continua are created according to the material types and applied to the computational regions. 3 physics continua with 1 sub-continuum are created in this simulation as follow:

- **Glass solid continuum** for glass layers in the windscreen/window
- **Foil solid continuum** for foil layers in the windscreen/window
- **Air fluid continuum** for air domain
    - **Ice fluid film continuum** for ice layer

The material properties for each continuum are listed in Table 3.2 The material properties of air are the default properties in the simulation while those of solids are given from the company. Note that, except for the air density, constant properties are used for the sake of simplicity. For the air density, the variation of temperature over the range of 60 ℃ could result in over 18% change of the air density, thus a constant value should not be used. Ideal gas law is therefore applied to simulate the variation of air density over temperature using the equation of state.

$$\rho = \frac{pM}{R_u T} \tag{3.1}$$

where M denotes the molecular weight of the gas and R_u denotes the universal gas constant.

For fluid film region, a step-function based on temperature is used to model material property change from ice to water at 0 ℃. Since no actual ice thickness was measured during the performance test, the initial ice thickness is set at 0.5 mm as estimated from the amount of water sprayed, assuming 10% is spilled and accounting for the water-ice density change. In addition, to avoid complex phenomena in the fluid film motion and allowing larger time step size to be used, the film viscosity remains at high value and the film is fixed on the windscreen/window surface for the whole simulation.

Table 3.2 Material properties set in physics continua.

Physic Continuum	Glass	Foil	Air	Fluid film	
				Ice	Water
Density [kg/m3]	2,500	1,000	Ideal gas law	920	
Dynamic viscosity [Pa.s]	-	-	1.85508 e-5	10 e+5	
Thermal conductivity [W/mK]	0.8	0.2	0.0260305	1.88	0.620271
Specific heat capacity [J/kgK]	750	1,980	1,003.62	2,040	4,181.72
Latent heat of fusion [J/kg]	-	-	-	334,960	
Liquidus/Solidus temperature [C]	-	-	-	0	

Next, the initial temperature of all regions is set to -16 °C, following the measurement from the performance testing. In addition, the initial velocity in the air continuum is specified at the domain inlet velocity (0.78 m/s) as the air circulation in the test domain was there since before the test began. This also improves the initialization and stability of the simulation.

For flow solver, segregated flow solver with segregated fluid temperature solver for fluid region and segregated solid energy for solid regions are selected due to its higher compatibility with non-compressible flow, lower memory usage and faster convergence rate compared to the coupled flow solver. Segregated solver solves for the pressure, velocity and energy separately in sequence. SIMPLE approach is utilized since it is more stable in simulation with high convective courant number compared to the alternative PISO algorithm. Second order upwind convection discretization scheme is used to obtain results with less numerical diffusion. For turbulence model, realizable k-epsilon Two-layer with Two-layer All y+ wall treatment is selected for the air continuum at first since they usually give acceptable results and stability in most types of flow and thus the most common model used in the industry. Note that the convective heat transfer due to buoyancy force is neglected and gravity is excluded from the simulation in this default setting.

Then, for the fluid film continuum, melting-solidification model are selected to allow the modelling of ice melting. In addition, the stabilize film thickness equation is enabled and the maximum film thickness of 5 mm is set as a boundary to ensure stability of the simulation.

For the time solver, implicit unsteady solver is selected for the transient simulation. However, to increase its stability, the simulation is run in steady state first until the residuals and tracked transport quantities, e.g. mass flow and temperature, stabilize. Continuity (for steady state simulation) and boundary initialization are also enabled to stabilize residuals in the initial phase. Afterwards, the simulation is then switched to implicit unsteady with 1st order temporal discretization scheme. From the recommended time step size of 1 – 5 s for heat conduction, 5 s time step size is used in this default setting for the sake of efficiency since the results are used mainly for comparison during the method verification. The proper time step size to yield time-accurate result will be determined later in the time solver verification section. Finally, a maximum internal step of 30 is set as a stopping criterion after observing that the residuals and other tracked transport quantities, converge well within each time step at this criterion.

3.2.6 Result monitoring

Data tracking and post-processing could be done in STAR-CCM+ altogether. Reports and monitors can be created to track specific functions at certain region while plots and scenes can be created to visualize the data as well.

In this study, probes are first created to represent the Ext and Int temperature probes on the windscreen/windows in the performance testing. These probes can be used to track solution data at these particular locations as shown in Figure 3.4.

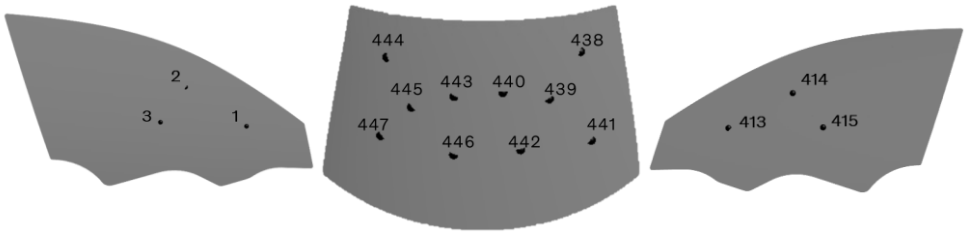

Figure 3.4 Temperature probe locations.

The placement of these probes is later verified with the windscreen image since there is no record of the exact location of these probes. The snapshot at 14 minutes testing time from the performance test and a simulation done following the CFD simulation setup are shown in Figure 3.5. Looking at the probe locations in relation to the ice melting pattern, it appears that they are fairly much in the same positions and therefore, should be valid for comparison in the study.

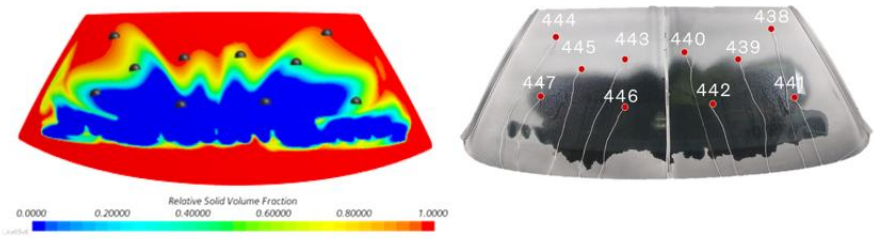

Figure 3.5 Probe locations verification.

Next, plots are created to monitor the following functions during the simulation. After the simulation, the time step triggered monitor of these functions is exported as a csv file for later data comparison.

- Residuals
- Surface averaged mass flow at inlets, outlets and through the vents to keep track of mass balance
- Surface averaged temperature at each vent outlets and each windscreen layers
- Temperature at the temperature probes

Scenes are also created to visualize the velocity (using cell velocity function) and temperature distribution pattern on the windscreen/window as well as the ice melting pattern (using relative solid volume fraction function), the wall y+ and the flow streamlines. A solution history data is also generated to record above functions over the course of the transient simulation. The data is recorded at every 2-minute of testing time and so animations can be created in the scenes from this solution history after the simulation.

3.3 Mesh independence study

Mesh independence study is of course the first study to be done since mesh size can affect both validity and efficiency of the simulation. Since the simulation is solved locally and stored in the face of each mesh, if the mesh is too rough, information can be missing and the solution might be less accurate. However, finer mesh requires larger computational resource and time. Consequently, the mesh size should be optimized so that it is relatively accurate and not too expensive computationally. In this study, 7 mesh sizes are examined to ensure that the results are not affected by the mesh influence as shown in Table 3.3. Note that A, B, C, D refer to different groups of surfaces in the geometry as listed in Table 3.4 and the mesh settings for different refinement levels according to company guideline are shown in Table 3.5.

Table 3.3 Mesh independence study settings.

Mesh	Domain mesh						Windscreen layer mesh	
	Polyhedral mesh				Prism layer	Mesh size (million cells)	Thin mesh	Mesh size (million cells)
	A	B	C	D				
1	-2	-4	-4	-4	-a	18.7	-5	Windscreen: 23.8 Windows: 5.4 each
2			-4	-5		25.3		
3			-5	-5		30.4		
4			-5	-6		45.8		
3.1			-5	-5	-b	59.9		
4.1			-5	-6		92.4		
3.2			-5	-5	-a	30.4	-4	Windscreen: 5.5 Windows: 1.9 each

Table 3.4 Groups of surfaces according to its proximity to the area of interest.

Group	Surfaces
A	Block walls, rear cabin floor
B	Seats, cabin floor, doors, B-pillar cover, steering wheel
C	Windscreen, window, roof, WEM cover, kaross
D	Defroster, A-pillar, IP covers

Table 3.5 Refinement levels and their mesh settings.

Refinement level	Polyhedral and thin mesh Target surface size : min surface size (mm)
-2	32 : 8
-3	16 : 4
-4	8 : 2
-5	4 : 1
-6	2 : 0.5
Refinement level	Prism layer Near wall thickness : total thickness : no. of layers
-a	2 mm : 4 mm : 2 layers
-b	0.05 mm : 4 mm : 8 layers

3.3.1 Polyhedral mesh study

First, the polyhedral mesh is refined in mesh 1 to 4. The simulations are run in steady state for the sake of efficiency and the converged results at 10k iteration are used for comparison. The simulation settings follow all settings in Section 3.2 except that the defroster inlet temperature is set to 315 K instead to also observe stability during ice melting. For all 4 meshes, the residuals indicate same level of stability and the domain mass balance falls within 1e-5 kg/s range as well. However, the velocity and temperature distribution pattern on the windscreen show noticeable sharpen shapes from mesh 1 to 3 as illustrated in Figure 3.6 Since mesh 3 and 4 results seem relatively similar, suggesting the mesh independency, they are therefore selected for the following prism layer mesh study.

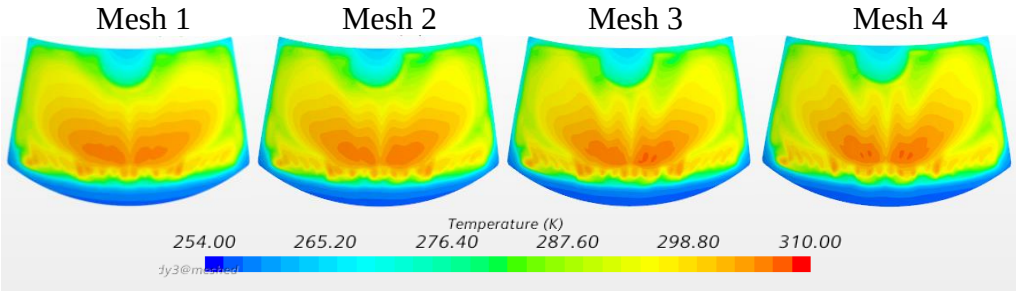

Figure 3.6 Temperature distribution pattern on the internal windscreen for mesh 1 - 4 respectively.

3.3.2 Prism layer mesh study

Mesh 3.1 and 4.1 are created in comparison to mesh 3 and 4 to verify the effect of prism layer. Previously with prism layer setting -a, the wall y+ on the windscreen ranges up to 55 indicating that the near-wall cell lies within all different layers of the boundary layer. With prism layer setting -b, the near-wall cell size is refined and now the wall y+ is below 5, indicating its location in the viscous sub-layer.

With the near-wall cells lying in different boundary layers, the magnitude of the cell velocity used to visualize the velocity distribution pattern on the windscreen changes. As the near-wall cells are closer to the wall with prism layer setting -b, the cell velocity approaches zero due to the non-slip wall condition. Thus, this cannot be used for comparison. However, the temperature distribution patterns on the windscreen for all 4 meshes still show similar results with only slight variation. In addition, except for probe 441, 443 and 447 that have temperature variation between 2 – 5 ℃, all other probes have less than 1 ℃ temperature variation between each mesh. This suggests mesh independent results for all 4 meshes. However, with prism layer setting -b, the residuals show a lot more fluctuation, signaling instability of the simulation. So, transient simulations are run to investigate this matter. Mesh 3 and 4.1 which are the coarsest and the finest mesh of this set are selected for investigation.

With transient simulation, the simulation stability does become an issue. For mesh 3, the simulation remains stable even when the time step is increased up to 5 s. All residuals and tracked quantities converge well within each time step. All absolute residuals are below 1e-6 except for energy and Tdr residual which converge below 1e-3 and 5e-5 respectively. In addition, the mass flow also balances out for the entire simulation.

However, for mesh 4.1, the residuals show more instability in the simulation. The simulation diverges at time step higher than 0.01 s, so the flow solver needs to be frozen to increase time step beyond that. At 0.1 s time step, the energy residual converges below 0.003. But when time step is increased to 1 s, the energy residual starts to behave erratically and can go up as high as 200. Although, it still decreases to converge below 0.03 in most time steps, in some, it cannot even reach 10 before the maximum internal step of 150 is reached. Thus, the time step is only increased up to 1 s and the simulation with 1 s time step with mesh 3 is run for comparison. This emphasizes the importance of mesh on the simulation stability. Proper mesh size should be found before running any simulation.

Nevertheless, regarding the results, less than 1 ℃ difference is seen in the defroster outlets temperature profile from each mesh. For the probes on the windscreen, the largest difference is seen at probe 444 with 1 and 4.7 minute earlier of the onset and the end of melting time in mesh 4.1. Although, for the rest of the probes, there are less than 1.5 minutes difference of the melting range. In addition, the ice melting patterns show only minor shape difference in the outer area as well. This suggests that mesh 3 result can be trusted to an extent and confirms the ability to deal with all y+ value of the All-y+ wall treatment selected.

In term of computational resource, mesh 3 is also considered more affordable as it takes about 1.5 hours to generate. For transient simulation, with the 960 computational cores used and 5 s time step size, mesh 3 simulation also only takes about 7 hours to run. Since mesh 3 results are mesh independence and its simulation is highly more stable and affordable, it is selected for the domain mesh setting.

3.3.3 Thin mesh study

Finally, mesh setting for solid layers is tested. Mesh 3.2 is run with reduced thin mesh size. Results show mesh independent result for temperature distribution profile on the windscreen. But the probe temperature profiles in mesh 3.2 show more instability and fluctuation. Mesh 3 is thus still the most preferable choice and used for the rest of the study. The final meshed computational domain is illustrated in Figure 3.7. Note that these thin mesh generation is the time-consuming part which takes over 5 hours to carried out. Nevertheless, it needs to be generated only once since its geometry does not change over different defroster designs, so it should not be too problematic.

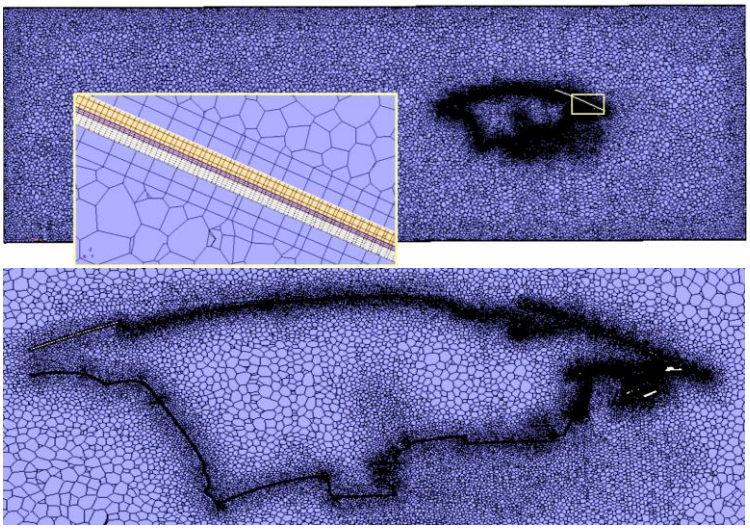

Figure 3.7 Final meshed computational domain.

3.4 Model verification

After the proper mesh size is selected, the next step of simulation method development is to study the effect of different models and solvers on the results and verify that the selected choices are suitable for the simulation. This study can be categorized into 3 main aspects including the time solver, flow solver and turbulence model respectively. The transient ice melting pattern and temperature profile from the probes and vent outlets are mainly used for comparison. In addition, the stability of the simulation, residuals, mass flow balance and velocity distribution pattern on the windscreen will be analyzed as well. The results are also validated against the performance test data if necessary.

3.4.1 Time solver study

Since transient simulation is required, the time solver settings can be critical to the result accuracy. For instance, since a transient simulation of about 40 minutes testing time is required, large time step size is preferable for the sake of efficiency. However, the flow solution usually requires much smaller time step size than the heat conduction solution in the solid and too large time step size can lead to missing information in the flow field and thus less time-accurate result. Therefore, the time step size is first optimized to find the largest time step size that still yields time step independence result. Since the typical time scale for fluid flow is about 0.01 s while the time scale for heat conduction in the solid entities are in the range of 1 – 5 s, simulations with time step size of 0.01, 0.5, 1 and 5 s are compared.

In addition, the effect of the temporal discretization scheme including the 1^{st} and 2^{nd} order discretization is studied as well.

3.4.2 Flow solver study

Next, since typical defrosting simulation is executed with a steady state flow simulation followed by a transient heat-up with the flow solver for both air and fluid film frozen, the effect of the frozen flow solver is studied. 2 simulations with and without the flow solver frozen are compared to investigate its effect on the results.

3.4.3 Turbulence model study

Turbulence can affect the momentum and heat transfer in the flow significantly and thus they certainly can affect the ice pattern on the windscreen. According to the literature review, 3 turbulence models, namely the realizable k-epsilon, LEB k-epsilon and SST k-omega, seem to have different suitability for this type of simulation. Therefore, simulations with these turbulence models are compared in this section in order to find the most suited model.

3.5 Boundary condition verification

Certain boundary conditions needed in the simulation are still ambiguous since they were not provided in the available test data. In this section, sensitivity analysis is performed on several boundary conditions in order to study the significance of their influence on the results. This primarily includes the flow and temperature settings of the defroster inlet, ice thickness, material properties and the external convection rate. 5 s time step size is first used to effectively examine if the setting is influential or not. If it is, 1 s time step size is then applied to obtain time accurate results for the validation against performance test data.

3.5.1 Defroster inlet velocity profile

Firstly, the temperature profile from the simulation with default settings and 1 s time step is validated against the test data as shown in Figure 3.8. Overall, the melting range is early compared to the test data. The heat conduction temperature slope is steeper but the melting time is longer than that in the test data, resulting in coincidentally match end of melting range at probe 440, 441, 442, 443, 446 in the middle region and on the driver side. Due to asymmetric melting pattern in the test data possibly from the presence of the driver, the melting range on the passenger side is about 1 - 2 minute delayed compared to the driver side and so the melting range of the simulation results in the passenger side is early compared to the test data. Additionally, the temperature rise in the liquid zone is also much faster than the test data, leading to 8 – 15 ℃ higher final temperature in all probes with varying degree of difference.

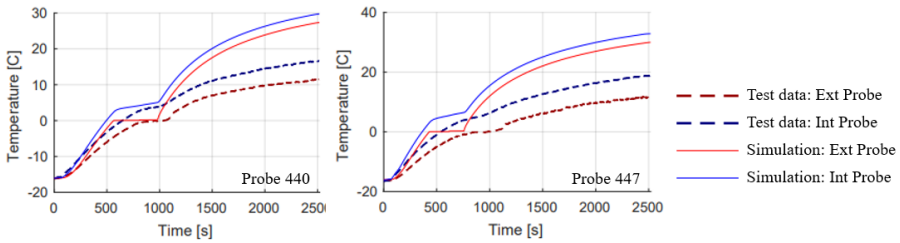

Figure 3.8 Representative temperature profile from probes on the windscreen from simulation and test data.

This early melting range and steep temperature profile could be resulted from overestimated mass flow rate at the defroster inlet. It should be noted that the company requirement of 100 l/s is actually at the HVAC unit inlet and there are certain leaks into other vent outlets aside from the defroster for Max defroster setting, so it is possible that the actual mass flow out of the defroster is less than the requirement 100 l/s. Since no actual flow rate was recorded from the test, the sensitivity analysis on the flow rate should be studied. 2 velocities of 6 and 2.67 m/s at the inlet are compared. 2.67 m/s velocity is estimated from comparing the mass flow rate measurement from the side defroster outlet in the simulation to an available test data and scale the defroster inlet velocity down to match it.

Later on, the effect of the velocity and turbulence profile out of HVAC unit is investigated since in reality, these profiles are not homogeneous as specified in the default settings. Another steady state simulation with HVAC unit and all air duct system is run separately to obtain the more accurate velocity and turbulence profile at the HVAC-defroster connection as illustrated in Figure 3.9. With these nonhomogeneous velocity profile, although the surface averaged velocity at the

defroster inlet is still about 6 m/s, the mass flow rate is reduced by almost 40%. If the velocity profile is homogeneous, it would have the velocity of about 3.545 m/s. 3 simulations with the homogeneous 3.545 m/s, with HVAC velocity profile and with HVAC velocity and turbulence profile are then carried out to examine the effect of each of these variables.

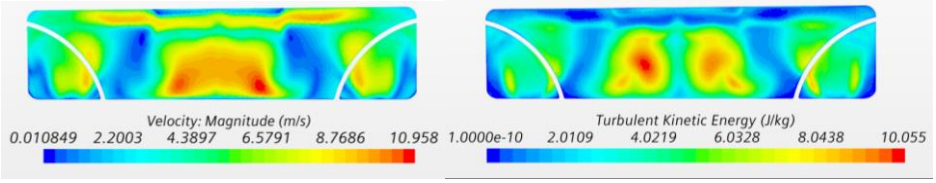

Figure 3.9 Velocity and turbulent kinetic energy profile at HVAC-defroster connection from HVAC simulation.

From the HVAC simulation, the local velocity components (i, j, k), turbulence kinetic energy and turbulence dissipation rate value at different locations on the monitor surface situated where the defroster inlet should be are exported. An x, y, z table of these values are then imported into the defroster simulation and applied as the defroster inlet boundary condition. Note that due to fixed velocity inlet boundary condition, these values are quite stable even though the inlet temperature is changing in a transient simulation. From observation, the temperature distribution across the surface is also homogeneous. So, the results from steady state HVAC simulation without energy solver should suffice.

3.5.2 Defroster inlet temperature profile

Since no mass is included in the defroster wall, the heat transfer through the duct wall is not included and can result in inaccurate temperature profile at the defroster outlets. According to the performance test data, the temperature profile at different defroster outlets show ± 3 – 4 °C variation from the temperature profile at defroster inlet as shown in Figure 3.10. However, in the simulation, the defroster outlets' temperatures are closer to the inlet temperature with only 2 – 4 °C lower temperature.

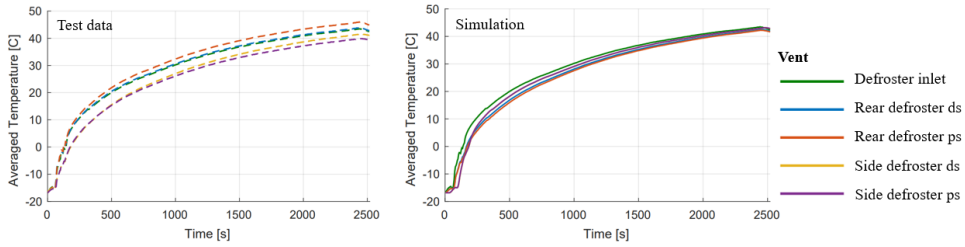

Figure 3.10 Temperature profile at defroster inlet and outlets from performance test data and simulation with default settings.

Thus, to investigate the effect of this variation on the result, the upper and lower boundary of these temperature profile in the test data which are the temperature profile from the rear defroster and side defroster outlet on the passenger side, are used as defroster inlet temperature for comparison.

In addition, since this simulation is intended to be used during the design phase, no test data will be available. So, the result sensitivity over the inlet temperature is studied in order to see if the temperature profile from previous test or other simulation with certain inaccuracy can be used as input data for later application or not. Defroster

inlet temperature profiles from a few defroster performance tests on different vehicle models are gathered and shown in Figure 3.11. Since Volvo VC and VB temperature profile are fairly similar, the temperature profile from Volvo VC is used for comparison to the default one from Volvo VA model.

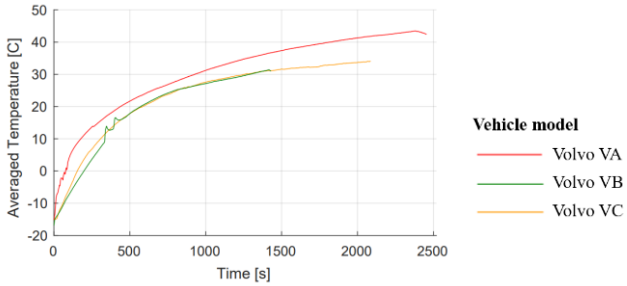

Figure 3.11 HVAC outlet averaged temperature profile during defroster performance test from different vehicle models.

3.5.3 Ice layer thickness

Next, since no ice thickness was measured during the performance testing, the ice thickness of 0.5 mm is estimated from the water amount sprayed. From the default simulation result, the melting time seems to be too long compared to the test data as seen in Figure 3.8. This could be from the overestimated ice thickness. The melting time in the test data is estimated to be only about 60% of those the simulation result, so simulations with the ice thickness of 0.3 mm and 0.5 mm are compared.

3.5.4 Inclusion of gravity

Since in this study the gravity is omitted for simplification, the heat transfer convection due to buoyancy effect is neglected. So, gravity is to be included to see if it has significant effect on the result or not. In addition, in a separate simulation, the viscosity of the water in the fluid film layer is reduced to the water property of 8.8871 e–4 Pa·s to allow water to flow after the ice has melted as well. So, the effect of water flow and absence of the water film are investigated.

3.5.5 Convection heat transfer

Then, the convection over the ice layer is further inspected in an attempt to improve the accuracy of the temperature profile result on the windscreen as well as to eliminate the dependency on the external air domain. With the ice layer interface to the external air domain removed and the surface thermal boundary condition set to convective heat transfer, the environment temperature and heat transfer coefficient (HTC) can be manually specified. The environment temperature is set to -16 ℃ according to the test room temperature, while the HTC is first set to 21.5 and 25 W/m^{2}K before and after melt with a user field function '(${RelativeSolidVolumeFraction} == 0) ? 25 : 21.5'. The 21.5 W/m^{2}K value is based on the Siple-Passel correlation [17] shown in equation (3.2) at 0.78 m/s velocity in the test room, while 25 W/m^{2}K value is arbitrarily stepped up to compensate for the heat going to the water film fixed on the windscreen. Later on, the HTC value is adjusted to suit the corrected defroster inlet velocity condition as well.

$$h = 12.12 - 1.16v + 11.6v^{1/2} \tag{3.2}$$

where v is the relative speed between object surface and air (m/s).

3.5.6 Temperature-dependent material properties

In default settings, constant material properties are used for the sake of simplicity. However, the effect of temperature dependent material properties should be verified. First, the change of density from ice to water is investigated by setting the density of the fluid film to change from 920 to 1000 kg/m^3 at 0 ℃.

Then, the effect of temperature-dependent dynamic viscosity, heat capacity and thermal conductivity of air and water are studied. Sutherland's law as shown in equation (3.3) and (3.4) is used to model the temperature-dependent dynamic viscosity and thermal conductivity of air since it provides fairly accurate prediction for air.

$$\frac{\mu}{\mu_0} = \left(\frac{T}{T_0}\right)^{\frac{3}{2}} \left(\frac{T_0+S_\mu}{T+S_\mu}\right) \tag{3.3}$$

$$\frac{\lambda}{\lambda_0} = \left(\frac{T}{T_0}\right)^{\frac{3}{2}} \left(\frac{T_0+S_k}{T+S_k}\right) \tag{3.4}$$

where S is the Sutherland constant. Subscript 0 indicates the value at reference temperature as specified in Table 3.6.

Table 3.6 Reference values used in Sutherland's law for predicting temperature-dependent dynamic viscosity and thermal conductivity of air.

T_0 [K]	μ_0 [Pa-s]	λ_0 [W/m-K]	S_μ [K]	S_k [K]
273.15	1.716 E-5	0.02414	111.0	194

Next, the default function in STAR-CCM+ given by the option 'polynomial in T' for air specific heat capacity is applied.

$$c_p(T) = 909.52824 + 0.32687268 - (1.0270822e-4)T^2 + (1.500574e-8)T^3 - (8.0228699e-13)T^4] \tag{3.5}$$

Finally, for water, the following data in Table 3.7 [18] is used to fit the temperature-dependent specific heat capacity and thermal conductivity.

Table 3.7 Temperature-dependent specific heat capacity and thermal conductivity of water.

Temperature [K]	Specific heat capacity [J/kgK]	Thermal conductivity [W/mK]
100	2040	1.88
273.15	4217	0.569
275	4211	-
280	4198	0.582
285	4189	0.59
290	4184	-
295	4181	0.606
300	4179	-
305	4178	0.62
310	4178	0.634

3.6 Geometry verification

From all the results in previous studies, the domain geometry is reconsidered. To improve the accuracy of the external flow field, the geometry is modified to make it more realistic. 4 other modifications are studied as listed in Table 3.8. First, the external air domain is modified to follow the dimensions of the test room with modified outlet at the orange surfaces as shown in Figure 3.12. Then, with the HVAC simulation, the defroster inlet has to be modified since the default inlet surface is extended down from the defroster duct system and so it does not fit with the HVAC unit in reality. Next, the simplified exterior of the cabin geometry is included to see if its effect on the external air flow field is significant or not. Finally, the rear section of the vehicle is also added and modified so the cabin interior becomes completely closed and separated from the exterior air domain with its own outlets in the rear part on the sides as shown in Figure 3.12.

Table 3.8 Geometry modification in each geometry model.

Model	Modified external domain	Modified defroster inlet surface	External car geometry	Modified car outlet
1	Original geometry			
2	/			
3		/		
4	/	/	/	
5	/	/	/	/

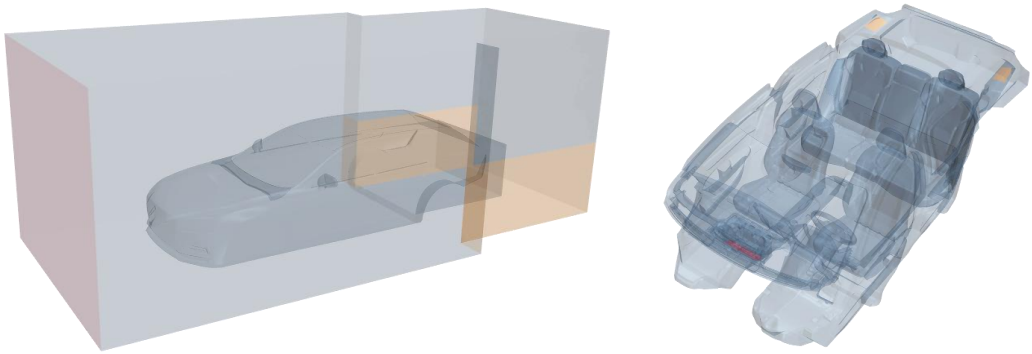

Figure 3.12 Volvo VA modified exterior and interior computational domain from geometry model 5.

3.7 Final simulation scheme validation

After the desirable simulation scheme is achieved from previous section, it would be interesting to also apply the developed simulation method on another vehicle model to test the reproducibility and trust level of the simulation. Another performance test data was available for Volvo VB and therefore it is used as the basis for computational domain in the final simulation scheme simulation study. Its geometry details resemble that of Volvo VA's modified version but with an adjusted exterior air domain since the performance test of this model was done in a different test room. The geometry is illustrated in Figure 3.13.

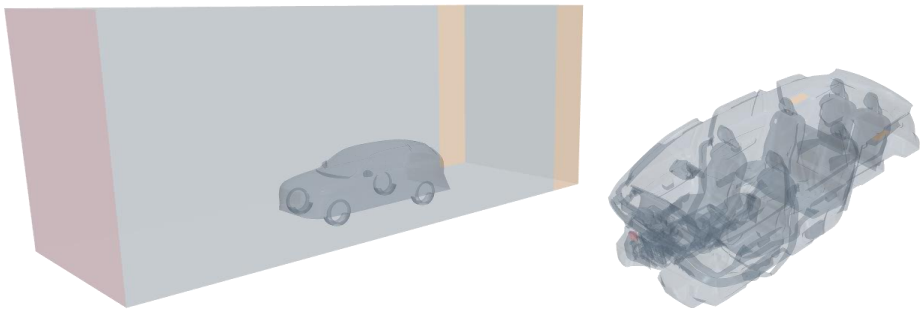

Figure 3.13 Volvo VB exterior and interior computational domain.

4 Result and Discussion

This chapter presents the simulation results and detailed discussion regarding each parameter studied in the order laid down in the methodology. The focus is to figure out important parameters and their effect on the result accuracy and the simulation efficiency.

4.1 Effect of time solver

4.1.1 Time step size

Optimal time step size is the first parameter identified in this study. Results from the simulations with time step size of 0.01, 0.5, 1 and 5 s are examined. Figure 4.1 shows the temperature profiles from representative Ext probes that exhibit the results with varying degree of difference. Note that the simulation with 0.01 s time step size is the last one simulated here and therefore it is simulated up to about 600 s only since it is apparent that its result does not differ significantly from that of 0.5 s time step size.

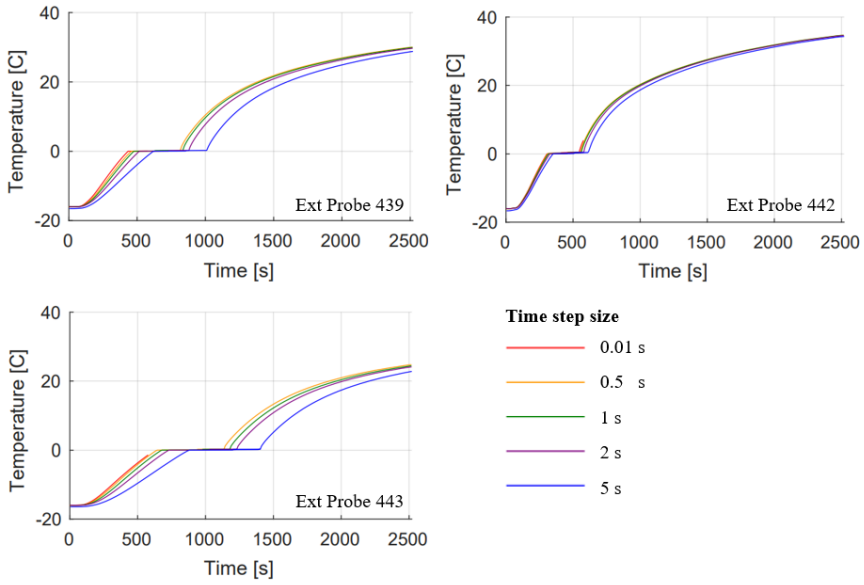

Figure 4.1 Representative temperature profile from Ext probes on the windscreen for different time step sizes.

These temperature data from Ext probes nicely illustrate 3 states of heat transfer including the linear heat conduction, the constant temperature melting range and the non-linear heat convection consecutively. It can be seen that for 0.01, 0.5, 1 and 2 s time step size, the results are fairly similar. The differences of the melting range in each of these time step sizes are only 10 s, 20 s and 60 s respectively. Barely any difference is seen in the ice melting pattern as well. This suggests that the air flow field from the defroster could be quite steady in spite of the temperature variation. This will be further verified with the flow solver study in section 4.2.

In contrast, for 5 s time step size, the temperature profile now shows noticeable difference in comparison to 1 s time step size result. There are 1 – 2 minutes delay of the melting range for probe 441, 442, 446 and 447 along the base of the windscreen and 2 – 4 minutes delay for the rest. The ice melting pattern also reflects the same observation as can be seen in Figure 4.2. In addition, 1 – 2 °C difference of the defroster outlets temperature profile are spotted as well. This delay in 5 s time step

size result indicates the inability to capture accurate changes in the system due to too large time step interval. 5 s time step size is therefore only used to quickly screen the parameter effect in this study for the sake of efficiency as its results still preserve the general trend. 1 s time step size is then applied if a time-accurate simulation is needed for validation against the test data.

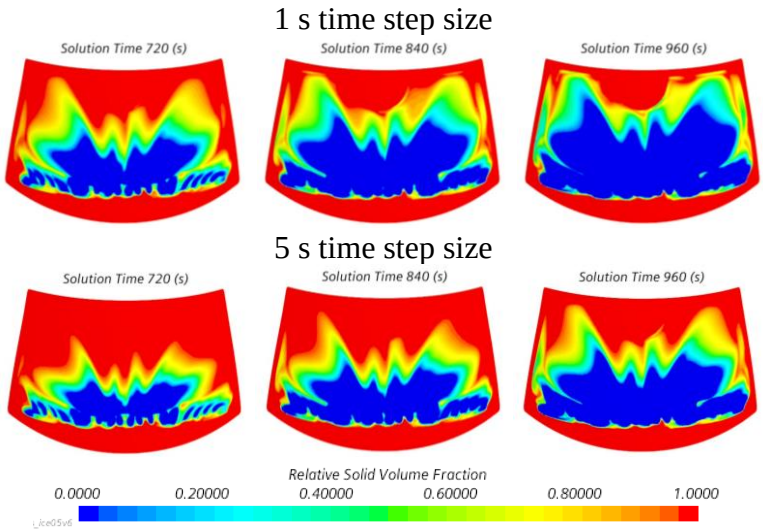

Figure 4.2 Ice melting pattern at different testing times from simulation with 1 and 5 s time step size.

Nevertheless, this conclusion on the time step size effect is not final. In the late phase of the study during the geometry verification, a contradiction to this conclusion was found. As will be discussed in section 4.9, with 4 other geometry modifications, the temperature profiles from the 5 s time step size simulations actually appear much closer to the 1 s time step size result of the original geometry with less than 1 minute delay of the melting range. Thus, the large delay seen in this section might not come from the physical unsteadiness of the flow field but rather some defect in the simulated geometry. Additional time step size study was then carried out on geometry model 5 with the time step size of 1, 5, 10 and 15 s.

The temperature profile results and the ice melting patterns illustrated in Figure 4.3 and Figure 4.4 confirm that the results are independent of the time step size setting up to 5 s value with less than 1 minute variation of the melting range and melting pattern between the 1 and 5 s time step size result. With time step size of 10 and 15 s, the melting range is 2 – 3 minutes delayed from that of the 1 s time step size. Slight difference is seen in the ice melting pattern as well but mostly not in the area of interest. This delay at such large time step size should be the consequence of exceeding the time scale of the conduction heat transfer in the solid region rather than the unsteadiness of the flow field. From these results, it can be concluded that in future application, this time step size dependency should be verified first as it could be influenced by the geometry. It is possible that time accurate results can be obtained at great efficiency with 5 s time step size. If less accuracy is acceptable, even 10 or 15 s time step size can be used. Note that the simulation starts to diverge at time step size above 20 s, so it should not be increased beyond this range. Since the solver time per time step is rather constant despite the variation of time step size, the simulation could be run within 4 hours with 10 s time step size, which is 10 times faster than the 1 s time step size simulation.

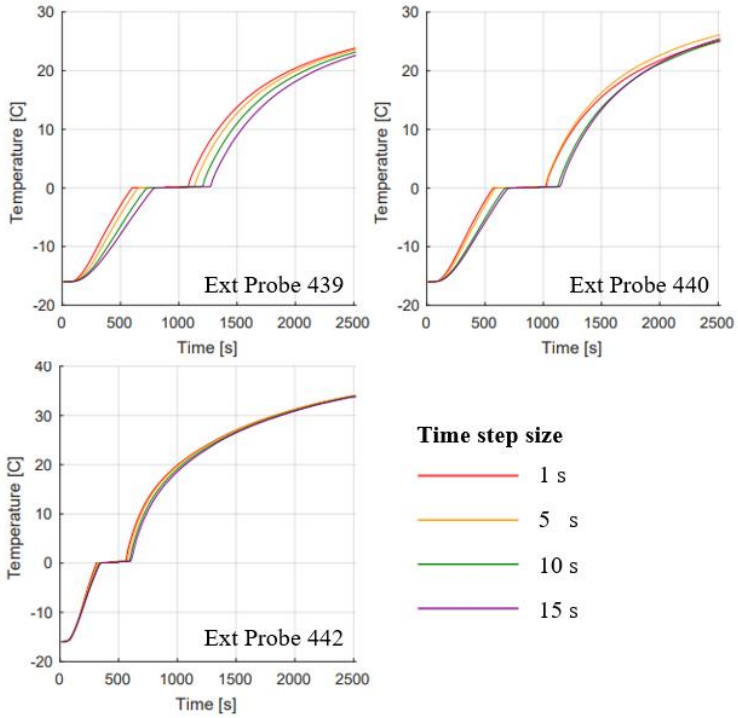

Figure 4.3 *Representative temperature profile from Ext probes on the windscreen with geometry model 5 and different time step sizes.*

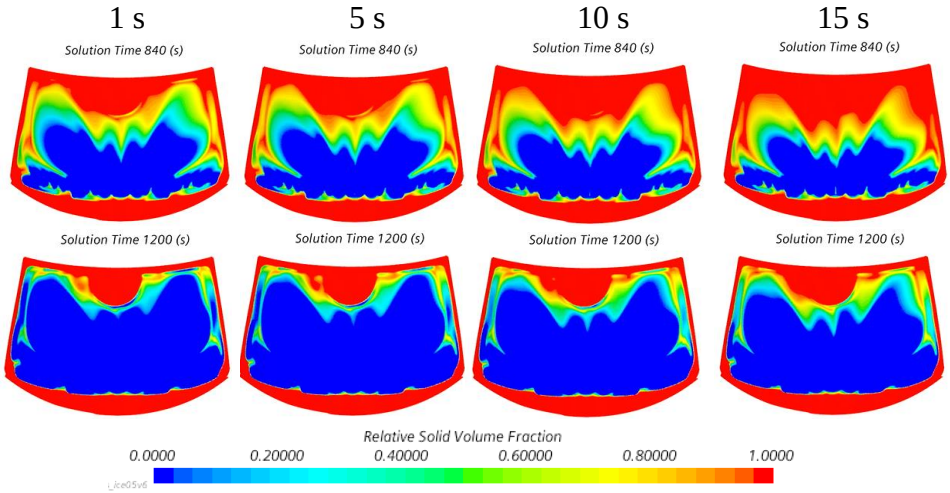

Figure 4.4 *Ice melting pattern at different testing times from simulations on geometry model 5 with different time step sizes.*

Note that if the transient simulation is run directly without the steady state (SS) initialization, the temperature profile only shows less than 0.5 ℃ difference in the initial 200 s of the testing time as shown in Figure 4.5. Therefore, if the simulation is stable, transient simulation can be directly initiated to save the computational time.

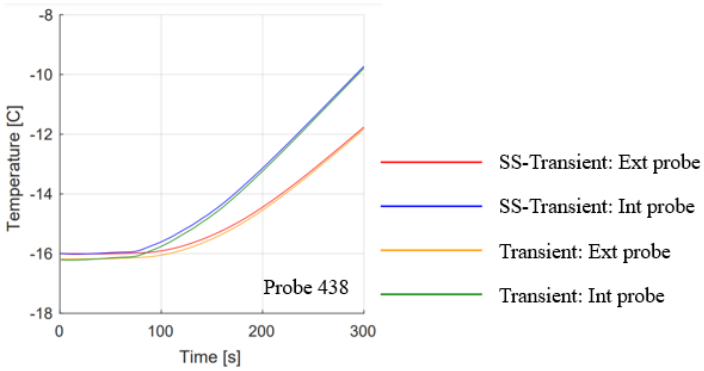

Figure 4.5 Representative temperature profile from probe on the windscreen from simulation with and without steady state initialization.

4.1.2 Temporal discretization scheme

Next, simulations with 1st order and 2nd order discretization scheme are compared. It seems that for the 2nd order scheme the x, y, z momentum and continuity residuals are lower for an order of magnitude. However, the simulation remains stable in both and as for the results, there are no noticeable effect on either the temperature profile or the melting pattern. Thus, this effect is considered insignificant and either scheme can be used.

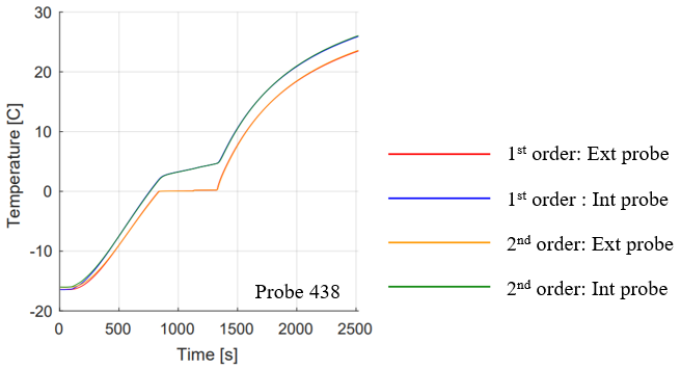

Figure 4.6 Representative temperature profile from probes on the windscreen for different temporal discretization schemes.

4.2 Effect of flow solver

Then, the conventional simulation scheme for the ice defroster is investigated. Running a steady state simulation to obtain the flow field and then solve for transient heat-up simulation with the flow field frozen shall reduce the complexity of the problem and the computational resources required. The simulation thus runs faster and more stable with the flow solver frozen. With omitted continuity and 3 momentum equations, the solver time per time step is reduced by 30 – 35% from 47 – 50 s to 33 – 35 s. Accounted for additional 0.5 – 1 hour to run the steady state simulation to convergence which takes about 2000 iterations, the total simulation time is reduced to 5 – 6 hours for 5 s time step size.

As for the results, only a slight difference of less than 1 °C of the defroster outlets temperature profile is seen. For the temperature profile at the probes on the windscreen, probe 441, 442, 446, and 447 along the base of the windscreen show insignificant difference, while the rest of the probes show 1 – 2 minutes difference of the melting range as demonstrated in Figure 4.7. Consequently, only minor difference is observed in the ice melting pattern as well as shown in Figure 4.8.

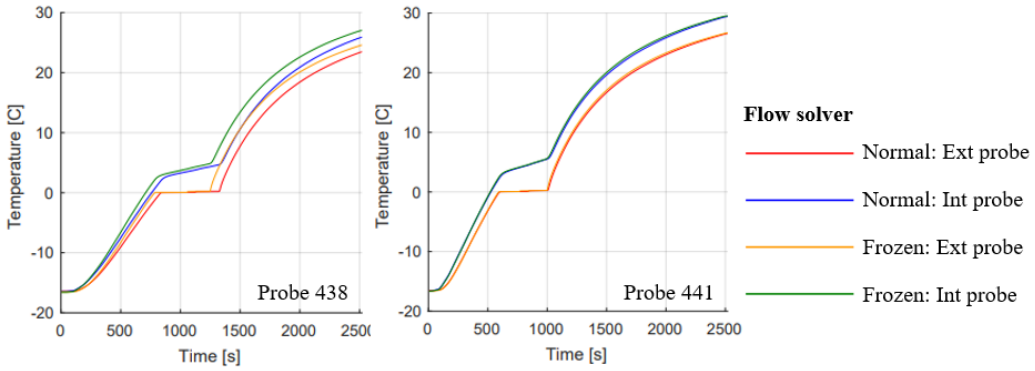

Figure 4.7 Representative temperature profile from probes on the windscreen for full and frozen flow solver simulation.

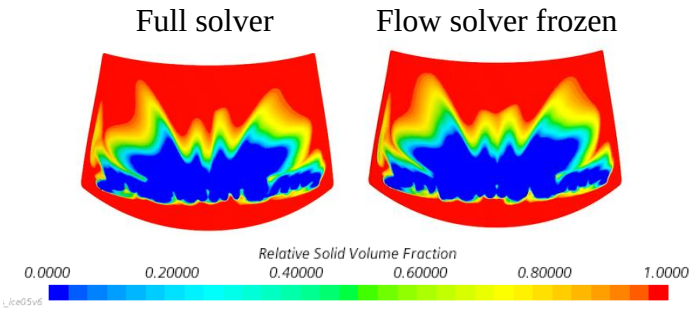

Figure 4.8 Ice melting pattern at 14-minute testing time from simulations with full and flow solver frozen.

It should be noted that freezing the flow solver can lead to an imbalance mass flow of up to 17 – 18% over time since the defroster inlet mass flow does not change with increasing temperature but the outlet mass flow does. Nonetheless, with the considerable small influence on the temperature profile and the ice melting pattern, it confirms that the flow field does stay quite steady over time and so freezing the flow

solver or increasing the time step size do not have significant effect on the result. 2 additional simulations are then run to test the setting combination that should maximize the simulation efficiency. A steady state simulation is run for 2000 iterations to obtain the converge flow field. Then, the transient simulations with 10 and 15 s time step size and flow solver frozen are executed with reduced number of iterations per time step to 15. These simulations are achieved within 2.5 and 2 hours respectively. Regarding the results, for the 10 s time step size, the melting range in the temperature profile is less than 2 minutes delayed from the 1 s time step size result and the ice melting pattern is still highly accurate as demonstrated in Figure 4.9. For the 15 s time step size, the result is now 3 minutes delayed and the difference becomes more obvious. Still, the selection between these 2 settings entirely depends on the required level of accuracy and efficiency needed. It can then be concluded that the flow solver could be frozen if the simulation efficiency is in favor or if the simulation is unstable and requires small time step size, for instance of the simulation with Mesh 4.1 setting. Although, with an additional 0.5 – 1 hour to run the SS simulation to convergence, it should only be considered when the 30% reduction in the transient simulation is worth it. Nevertheless, since the method is to be verified in this study, accuracy is favored and so the flow solver stays unfrozen.

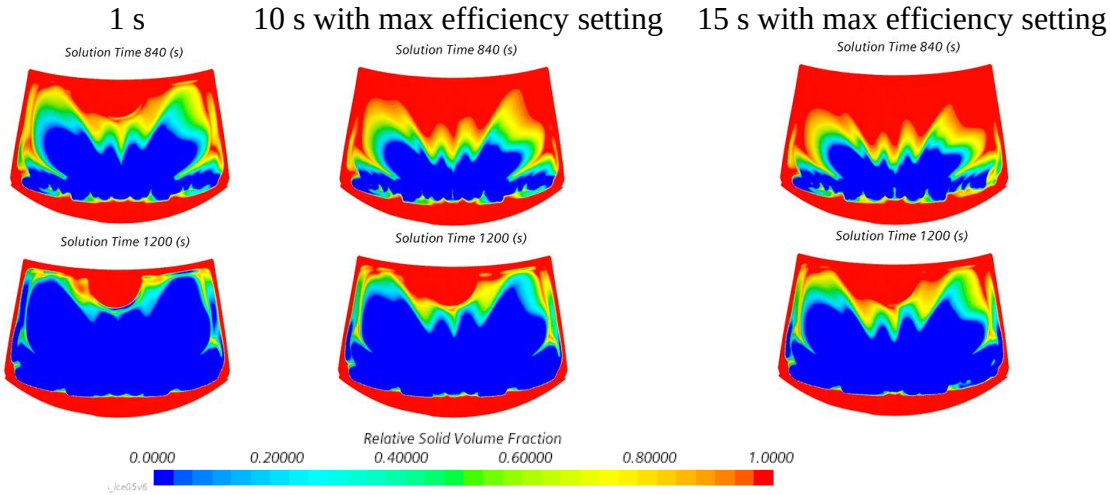

Figure 4.9 Ice melting pattern at different testing times from simulation with different time step size and flow solver setting.

4.3 Effect of turbulence model

3 turbulence models including the realizable k-epsilon, LEB k-epsilon and SST k-omega are selected for study. The results are discussed in this section.

First, for RKE and LEB-KE model, the simulations remain stable and the results show no significant differences. LEB-KE model leads to less than 1 minute earlier melting range and a bit steeper temperature rises in the convection zone in some probes when compared to that of the RKE model as illustrated in Figure 4.10. Additionally, there are only less than 1 ℃ difference in the defroster vent outlets temperature profile as well. The velocity distribution and ice melting pattern also show only minor variation in the upper and side region of the windscreen as can be seen in Figure 4.11 and Figure 4.12. Figure 4.11 illustrates the velocity distribution pattern on the internal side of the windscreen from different turbulence models. It appears that the impingement shape resembles butterfly as expected for all models. The velocity is highest at the center near the base of the windscreen where the air from the rear defroster outlet is directed to. Then, it spreads outward and upward to the rest of the windscreen while the area along the base of the windscreen is taken care of by the air from the front defroster outlet. There are also dead zones with almost zero velocity near the WEM cover at the top center, which leads to slower ice melting around that area in both performance test and the simulation result. For both KE models, the flow distribution pattern is stable throughout the simulation with only minimal increase over time.

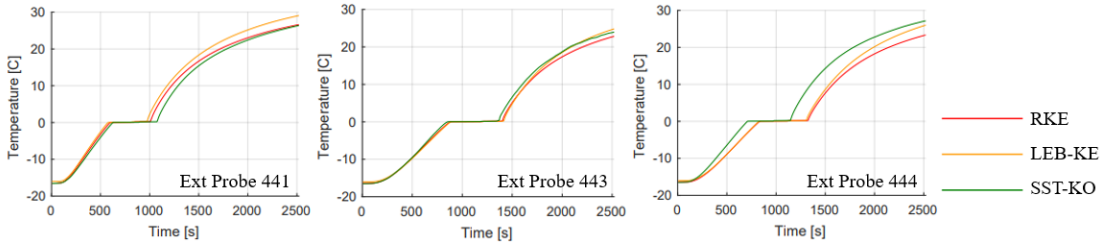

Figure 4.10 Representative temperature profile from Ext probes on the windscreen for different turbulence models.

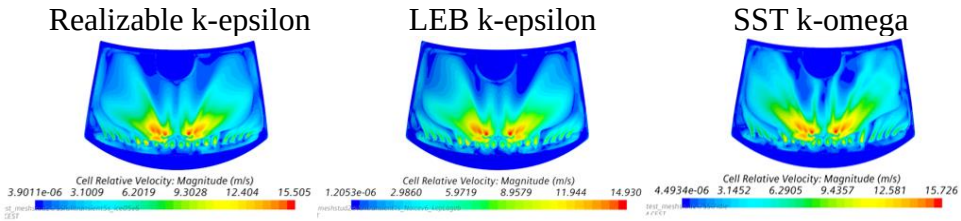

Figure 4.11 Velocity distribution pattern at 2-minute testing time for different turbulence models.

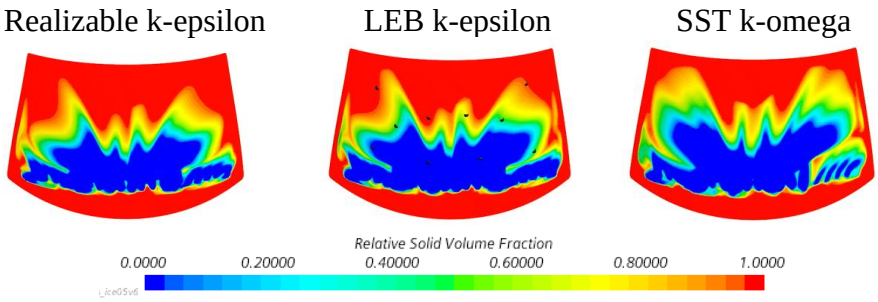

Figure 4.12 Ice melting pattern at 14-minute testing time from simulations with different turbulence models.

Now, for SST-KO model, the result differs quite evidently from those of KE models. Compared to RKE model, there are 1 – 3 minutes earlier of the melting range for probe 438, 440, 444, and 445 in the upper region, although, for the rest of the probes, there are less than 1-minute difference. There is also much more fluctuation in the velocity distribution pattern over time in SST-KO model and the velocity distribution pattern is noticeably distinct from the others. And as anticipated from this result, although all turbulence models still lead to roughly the same area of ice melted overall, the shape of the melted part in SST-KO model is quite irregular and asymmetric and is clearly different from those of the KE models as shown in Figure 4.12. The choice of turbulence model thus can affect the ice melting pattern on the windscreen significantly.

Moreover, by examining the residuals of the SST-KO model, it turns out that the film momentum residuals are 1 – 2 order of magnitude higher than that of KE models, while the energy residual also converges in higher range as well (around 5 compared to around 1). This signals the instability of the simulation as can be seen in unstable temperature profile in some probes. Hence, despite the model modifications, SST-KO model is still less stable than KE models. Since the ice melting pattern of the SST-KO model does not show substantially more resemblance to reality compared to those of KE models, KE models are still the preferable choice here. Since both RKE and LEB-KE result are fairly similar, the default RKE model remains the selected choice in this study.

4.4 Effect of defroster inlet velocity profile

Defroster inlet velocity is verified in this section. 2 velocities of 6 and 2.67 m/s are first tested out. 1 s time step size is applied since time accurate data is required. It appears that there are less than 1 ℃ difference of defroster outlets temperature profile between these 2 inlet velocities. Compared to the 6 m/s condition, except for probe 442 and 446 in the center with only 2 – 3 minutes delay of melting range, the rest of the probes exhibit 3 – 8 minutes delay with 2.67 m/s condition as illustrated in Figure 4.13. This leads to more accurate heat conduction slope, melting range (except for probe 440 – 443) and overall temperature range with 2.67 m/s inlet velocity when compared to the test data. However, the ice melting pattern in 2.67 m/s condition becomes rather delayed from the test result as seen in Figure 4.14. This points out the need for the more accurate inlet velocity profile and so, the velocity profile from HVAC simulation is further investigated.

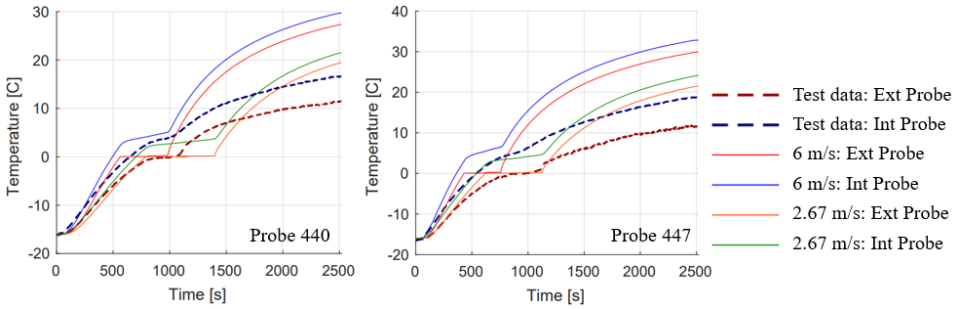

Figure 4.13 Representative temperature profile from probes on the windscreen from simulations with 6 and 2.67 m/s defroster inlet velocity and test data.

From the HVAC simulation, it is found that the mass flow rate is reduced to an equivalent homogeneous inlet velocity of 3.545 m/s. 3 simulations with the homogeneous 3.545 m/s, with HVAC velocity profile and with HVAC velocity and turbulence profile are therefore compared. Geometry model 5 is used in these simulations since the HVAC simulation is done in the late phase of the study. 1 s time step size is applied since time accurate result is desirable. Note that if the inlet boundary condition is provided in term of mass flow rate, a fix mass inlet boundary condition can be used as well. It has been verified that it does not yield different result from fix inlet velocity.

As for the results, less than 1-minute difference of the melting range is seen in the temperature profiles from all 3 simulations as illustrated in Figure 4.15. The temperature range is also closer to the test data. The ice melting patterns exhibit similar ice melted area in all these simulations as shown in Figure 4.14. However, a different pattern is seen with the HVAC turbulence profile and it seems to be more accurate with smoother melted region. This emphasizes the influence of turbulence settings at inlet boundary condition. Although, the result from simulations without HVAC turbulence profile display more obvious curves and shapes that are quite interesting. So, it might be worthwhile to check both conditions in future application. As for the simulation with homogeneous and non-homogeneous velocity profile from HVAC, only minor differences are observed. So, either of these can be used depend on the data availability. Regardlessly, since this part of the study was carried out quite late, the defroster inlet velocity of 6 m/s is still used in most of the subsequent studies.

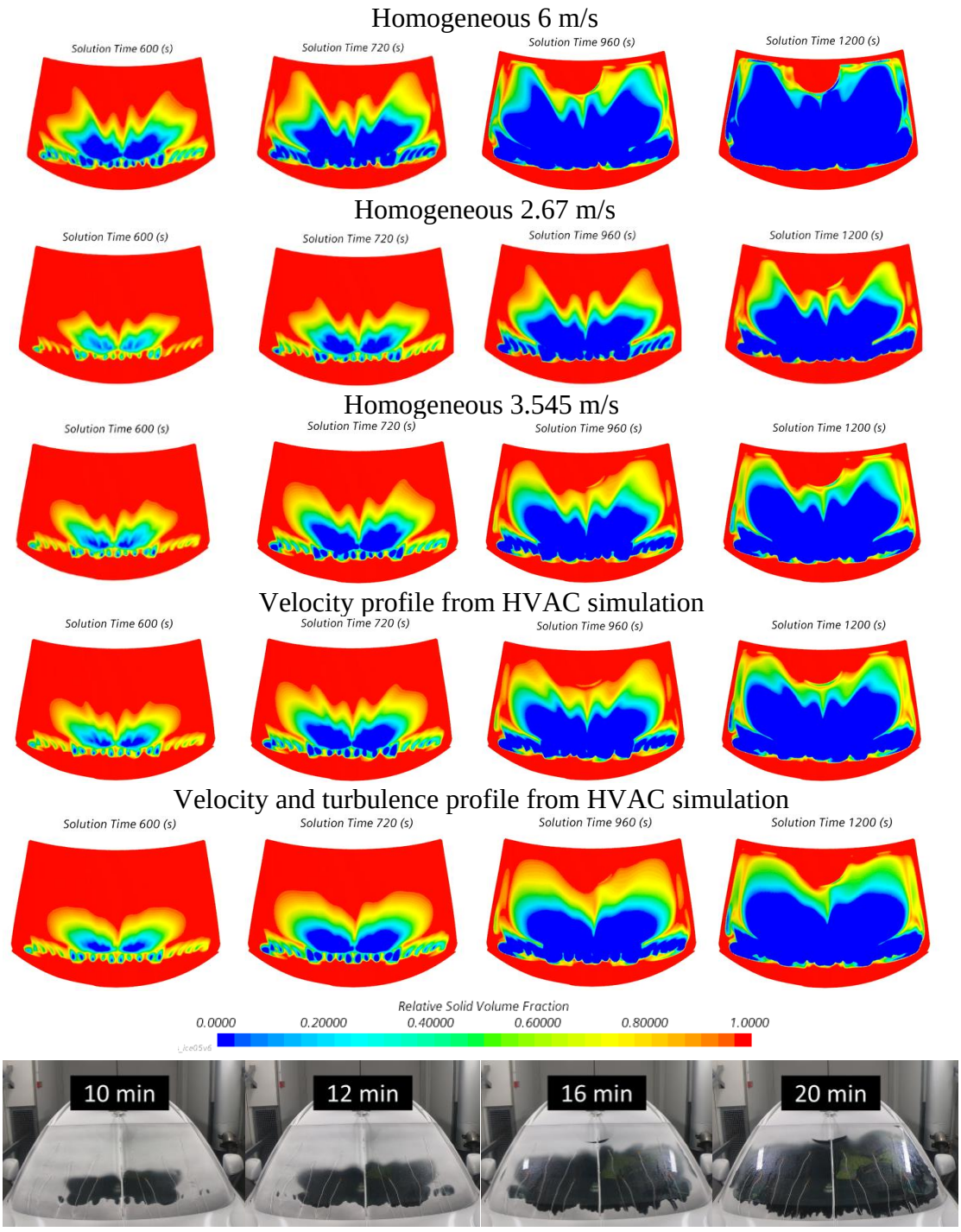

Figure 4.14 Ice melting pattern at different testing times from simulations with different defroster inlet velocities and the performance test.

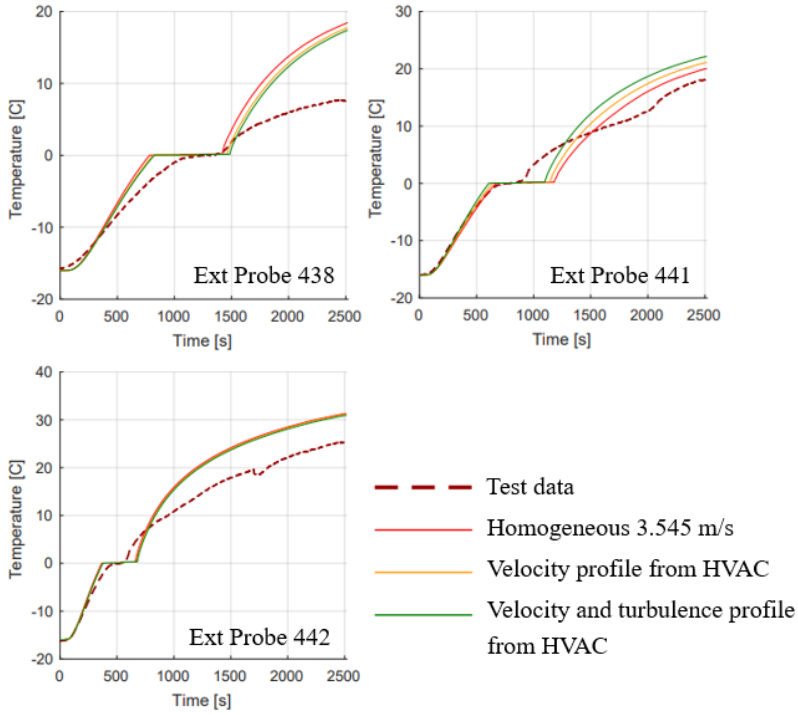

Figure 4.15 Representative temperature profile from Ext probes on the windscreen for different defroster inlet velocity profiles.

Additionally, the ice melting pattern on the side windows are examined here as well since this boundary condition provides quite an accurate data. Figure 4.16 shows the comparison between the 3 simulations with different defroster inlet conditions. It seems the effect of this parameter is not as obvious on the side windows since the flow has longer distance to progress. All simulations demonstrate relatively similar pattern here. The validation with performance test data at each testing time can then be seen in Figure 4.17. The results are considered satisfyingly accurate as well. Note that if the result from side window is not required, it can be excluded from the simulation with no effect on the result on the windscreen.

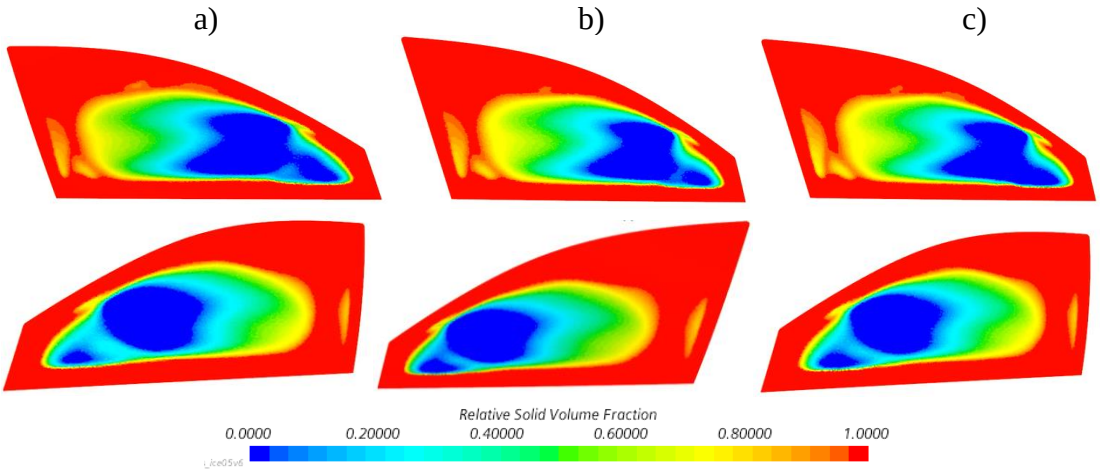

Figure 4.16 Ice melting pattern on front side windows at 20-minute testing times from simulation with defroster inlet velocity set as a) Homogeneous 3.545 m/s b) Velocity profile from HVAC and c) Velocity and Turbulence profile from HVAC.

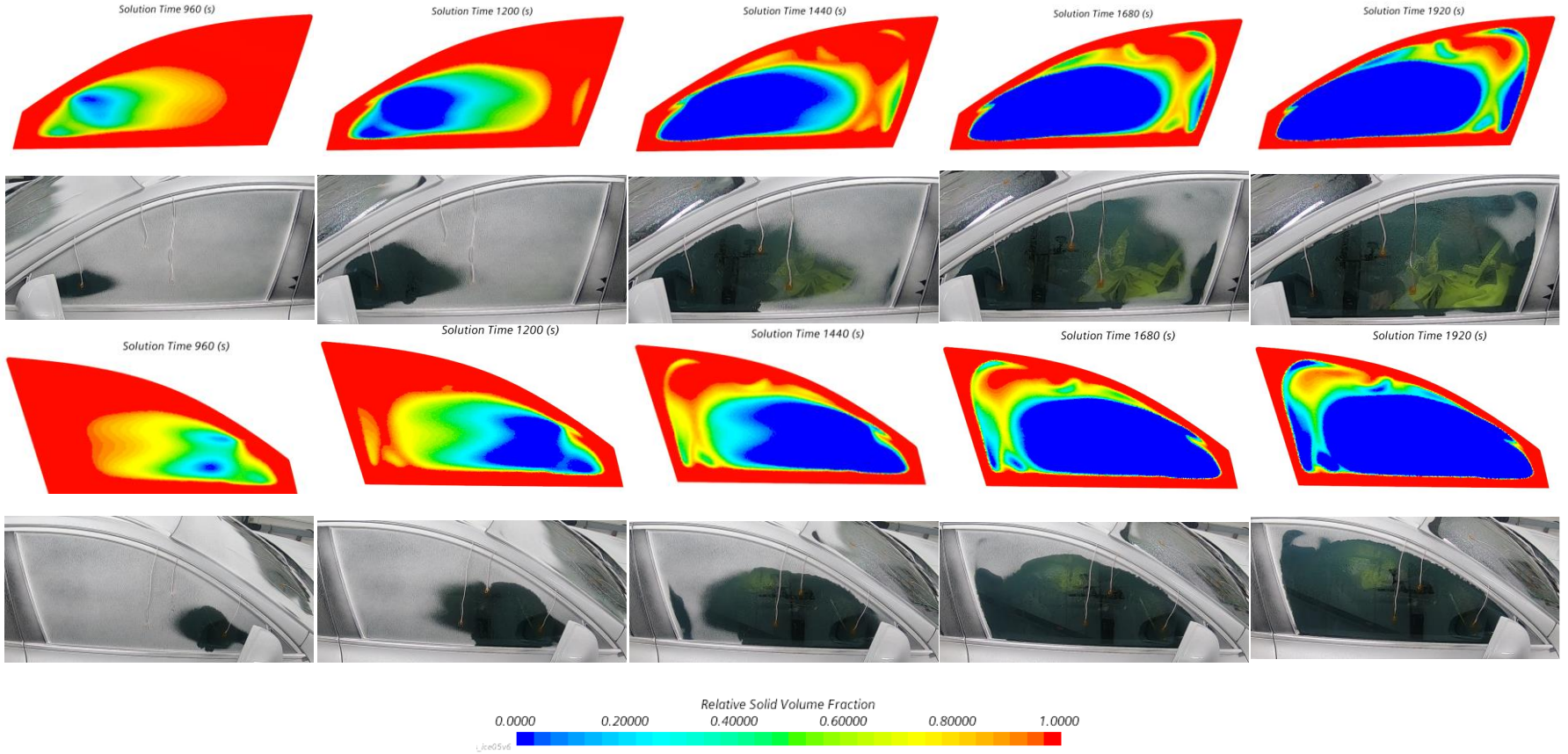

Figure 4.17 Ice melting pattern on front side windows at different testing times from simulation with velocity profile from HVAC set as defroster inlet boundary condition and performance test.

4.5 Effect of defroster inlet temperature profile

Next, the temperature profile from the rear defroster outlet and side defroster outlet on the passenger side (T-rear ps and T-side ps) as well as the average temperature profile from HVAC outlet of Volvo VC (T-HVAC VC) are used as defroster inlet temperature in order to investigate the sensitivity of results over this parameter. Figure 4.18 illustrates the representative temperature profile from one of the external probes on the windscreen since same behavior is seen in all probes.

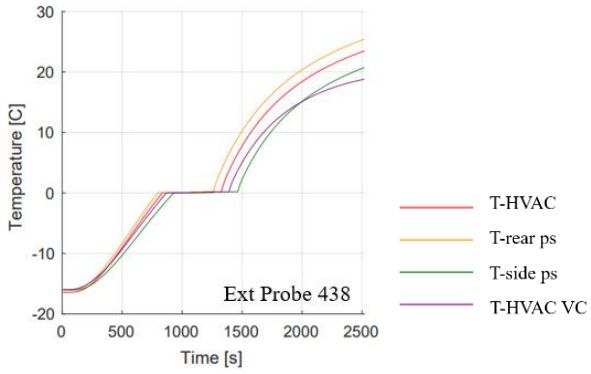

Figure 4.18 Representative temperature profile from Ext probe on the windscreen for different defroster inlet temperature profiles.

It appears that the variation between the melting range of the simulation with default T-HVAC profile to the one with T-rear ps, T-side ps and T-HVAC VC are 1, 2.5 and 1 minutes respectively. With higher temperature in T-rear ps profile, the melting range is shifted earlier, while with lower temperature in T-side ps and T-HVAC VC profile, the melting range is delayed. The ice melting pattern also reflects the same observation without change of the melted shape as shown in Figure 4.19. Since the T-rear ps is the main defroster outlet that directs flow to the windscreen and its result does not differ immensely from that of the T-HVAC simulation, it implies that the alteration of defroster outlets' temperature in the simulation from the test data (shown in Figure 3.10) is acceptable. It is therefore not necessary to model the heat loss through the defroster duct and T-HVAC profile remains the defroster inlet temperature profile in this study. Finally, since the results from all these temperature profiles are still relatively close, it indicates that the results can tolerate 5 – 10 ℃ variation in the inlet temperature profile and it should therefore be acceptable to use the temperature profile from previous test data or HVAC simulation as input in the future application. This data might be useful for energy optimization in the HVAC unit in the future as well.

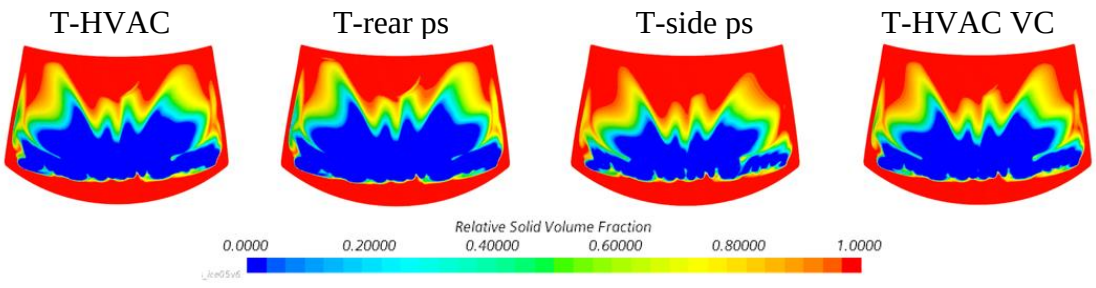

Figure 4.19 Ice melting pattern at 16-minute testing time from simulations with different defroster inlet temperature profiles.

4.6 Effect of ice layer thickness

Next, the effect of ice layer thickness is studied. The defroster inlet velocity of 2.67 m/s and 1 s time step size are used since the melting range matches better with the test data (before HVAC velocity profile was obtained) and time accurate result is required. It can be seen in Figure 4.20 that the ice thickness only affects the melting time and the effect is quite proportional. For the ice thickness of 0.3 mm, the melting time is reduced to about 60% of that in 0.5 mm as expected, resulting in 3 – 4.5 minutes earlier melting time in most probes (2 minutes for Probe 442 and 446). The ice melting pattern also reflects the same behavior as illustrated in Figure 4.21. This leads to better resemblance to the temperature profiles from the test data, although since these are simulations with 2.67 m/s inlet velocity, they are still quite delayed.

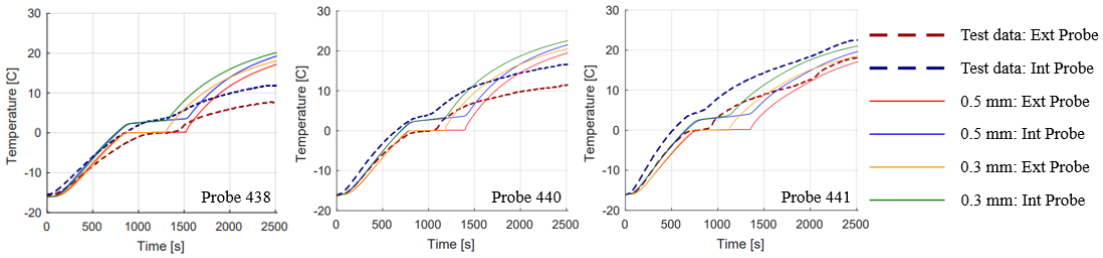

Figure 4.20 Representative temperature profile from probes on the windscreen for different ice thicknesses.

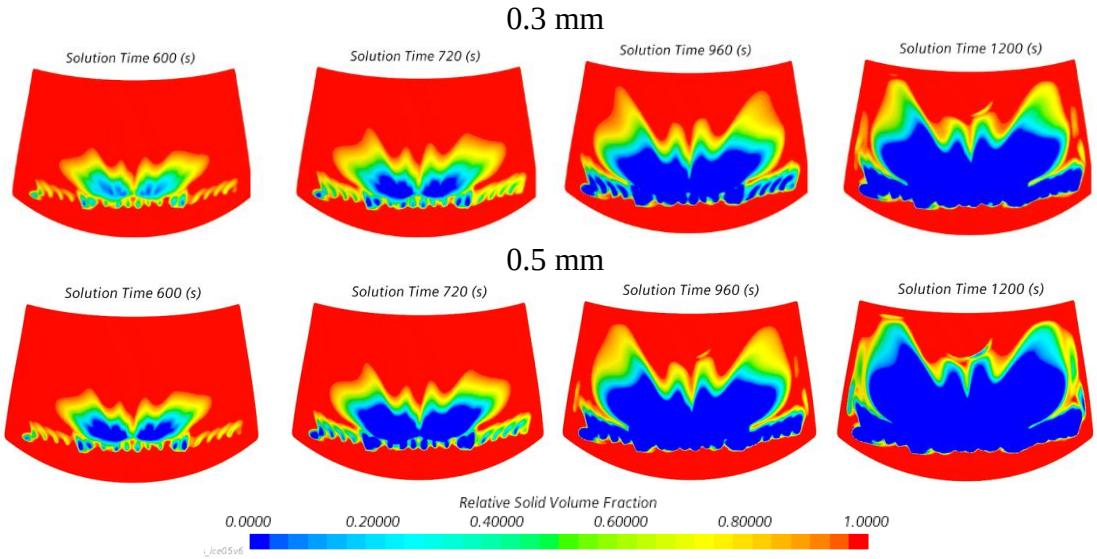

Figure 4.21 Ice melting pattern at different testing times from simulations with different ice thicknesses.

The result thus suggests that the default ice thickness might be overestimated. This may arise from water overspill, the interference of the probe presence at the measurement location or the uneven ice thickness on the screen. Since no actual ice thickness was measured, this hypothesis cannot be verified. As this parameter has considerable influence on the results, the ice thickness should be measured during future tests so the simulation scheme could be further improved. For this study, the ice layer thickness of 0.5 mm is maintained to be on the safe side since the ice thickness of 0.3 cannot be firmly validated.

4.7 Effect of gravity

In this section, the gravity is included to see if the buoyancy effect has significant influence over the results or not. It turns out that, for simulations with the water film still fixed on the windscreen, the gravity fastens the melting range in all probes for less than 1 minutes. Barely any difference is seen in the ice melting pattern as well. Thus, it appears that the natural convection is negligible compared to the forced convection in this scenario and the gravity can be safely excluded.

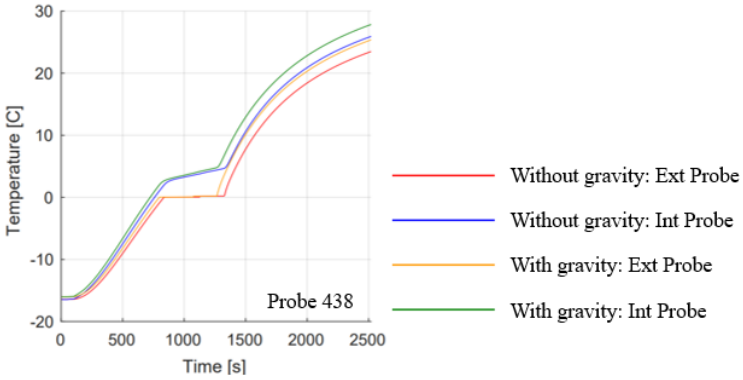

Figure 4.22 Representative temperature profile from probes on the windscreen illustrating the effect of gravity.

Then, is a separate simulation, the effect of water movement in the film layer is examined with the viscosity in the ice layer reduced after melt to allow the water to flow down with gravity. The ice thickness of 0.3 mm and defroster inlet velocity of 2.67 m/s are applied here since it was done during the ice thickness study. For the simulation without the gravity, 1 s time step size is used, while for the simulation with reduced viscosity, 0.1 s time step size is used due to stability issue.

For simulation with reduced viscosity, at around 9 minutes of testing time when complete melting (0 solid volume fraction) is reached in the ice layer and the fluid in film begins to move, the energy, film continuity and film momentum residuals spike up significantly. Mass flow at the car outlet and the temperature at the outlet of the defroster vents also suddenly increase. The outlet mass flow eventually balances out with the inlet mass flow after 2 minutes testing time, but the spike in the defroster outlets temperature results in 1 – 2 ℃ higher temperature compared to the simulation without gravity. However despite this instability, the temperature profile from probes on the windscreen still show only 1 – 2.5 minutes delay with the gravity as seen in Figure 4.23. Notice that there is an additional curve seen in the temperature profile after the melting range in probe 441 as well, possibly from the flow of water. Now for the ice melting pattern, except for the additional melting seen on the lower region of the windscreen from water flowing down, only slight difference is observed as illustrated in Figure 4.24. Hence, with this minimal influence, the inclusion of the flow in water film is not vital. Considering the stability issue and much reduced efficiency due to time step size limitation, it is therefore not recommended.

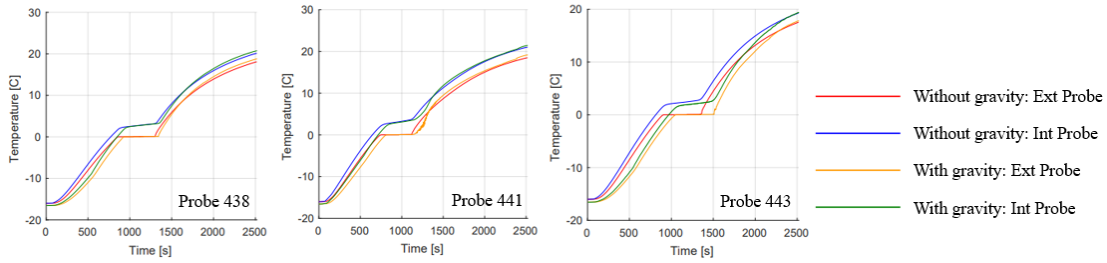

Figure 4.23 Representative temperature profile from probes on the windscreen illustrating the effect of gravity and viscosity reduction.

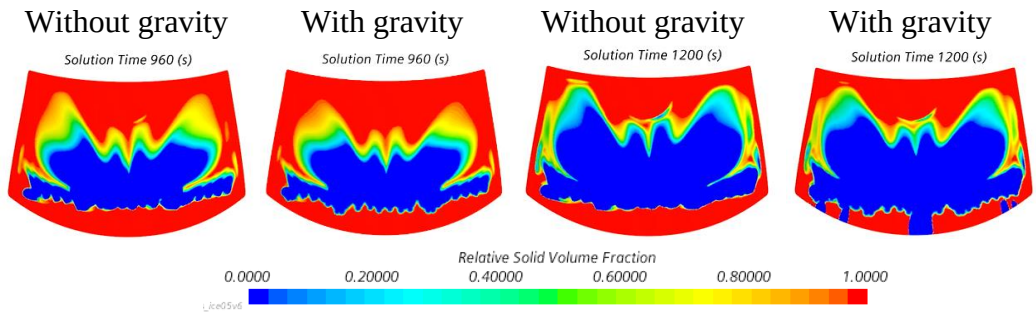

Figure 4.24 Ice melting pattern at 16- and 20-minute testing time from simulations without and with gravity effect and viscosity reduction.

4.8 Effect of external convection rate

Next, the heat transfer coefficient (HTC) is manually set on the upper boundary of the ice layer in an attempt to improve the temperature profile accuracy. First, the estimated HTC of 21.5:25 W/m^{2}K before and after the ice melted are tested. The ice thickness of 0.3 mm is used since it matches the test data better. Note that the default defroster inlet velocity of 6 m/s is used here since the 2.67 m/s result is too delayed and the HVAC velocity profile has not been obtained. The simulation is executed at 1 s time step size to achieve the time accurate solution.

It can be seen in Figure 4.25 that the HTC greatly affect temperature slope and the melting range. It appears that this estimated value of HTC does lead to quite an accurate temperature profile in most probes, except for probe 443 as shown in Figure 4.25. The large delay observed in probe 443 can be traced back to the ice melting pattern result. As illustrated in Figure 4.26, it appears the solid in the upper region melts much slower compared to the interface convection simulation. Probe 443 is installed in this region and therefore a large delay is seen in its temperature profile. The cause of this delay might be from the overprediction of HTC value in this region due to the homogeneous setting or from the fixed convection temperature at -16 °C since in reality, when the ice layer is heated up, it also heats the air above it as well which then flows upwards towards this region.

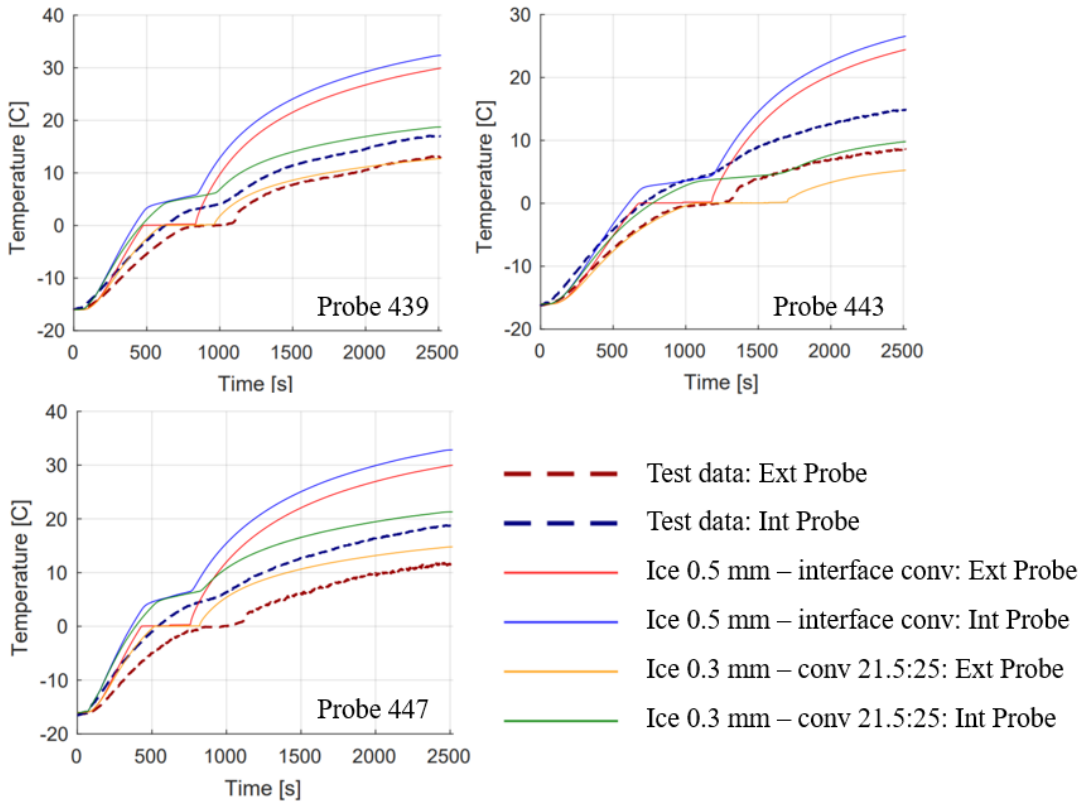

Figure 4.25 Representative temperature profile from Ext probes on the windscreen with HTC of 21.5:25 W/m^{2}K set at the upper ice layer boundary in comparison with the test data.

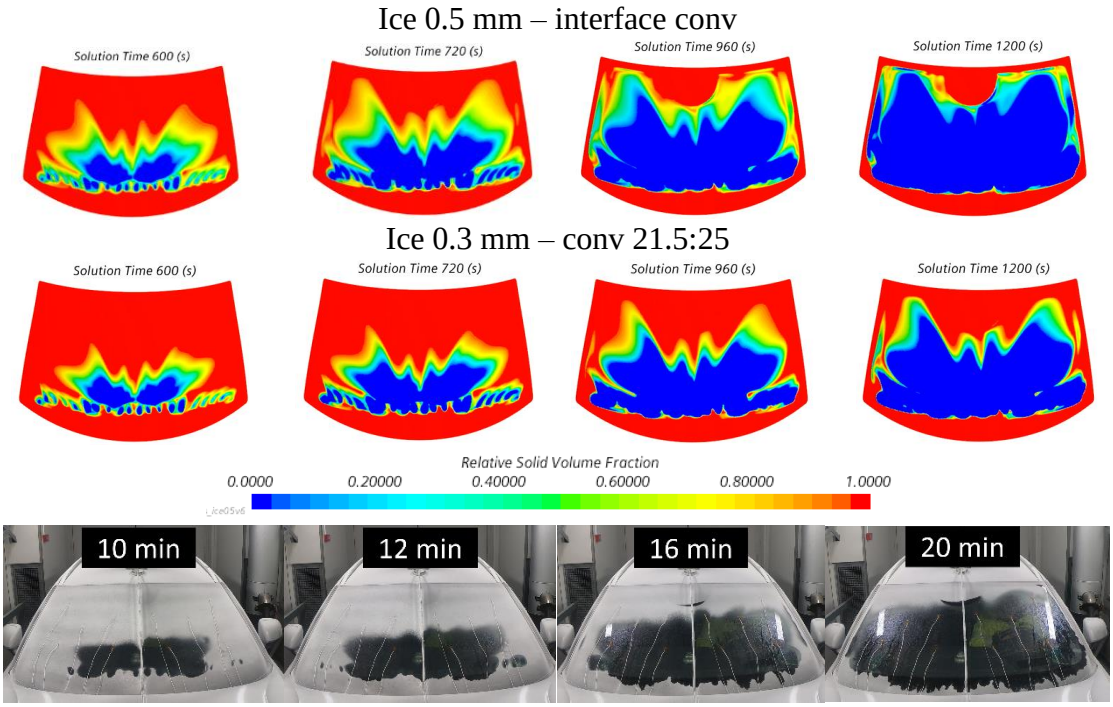

Figure 4.26 Ice melting pattern at different testing times from simulations with interface convection and manually set convection and performance test.

Afterwards, when the accurate defroster inlet profile is obtained from HVAC simulation, the HTC is reinvestigated. The simulation is executed in geometry model 5 with the ice thickness of 0.3 mm and 5 s time step size which already yields time accurate results.

With the reduced mass flow of almost 40%, the estimated convection rate of 21.5:25 W/m^2K is now highly overrated, leading to a substantial delay in the temperature profiles as illustrated in Figure 4.27. Thus, the HTC is tuned to the value of 10:15 W/m^2K instead. With this value of HTC, except for 4 – 5 minutes delay in probe 440 and early in probe 444 and 445, the temperature profile is highly improved and correspond well to the test data. The ice melting pattern also shows much better correlation with the result from interface convection simulation for both the windscreen and front side windows as shown in Figure 4.28 and Figure 4.29. Most of the delay remains in the upper and side area for the windscreen and in the area near the B-pillar for the front side windows which are all out of the region of interest.

From this result, it appears that the HTC value is dependent on the energy supplied to the windscreen and thereby the defroster flow rate. It might also depend on other parameters as will be discussed in section 4.11 as well, when it is verified on another vehicle model. So, it seems the HTC need to be tuned with caution before the result can be trusted. Nevertheless, if it is tuned correctly, this scheme can be useful for the simulation efficiency. Since the external air domain no longer affects the result in this scheme, its size can be largely reduced to barely cover the windscreen and front side window just so to support the insertion of the ice layer. The meshing time can be reduced by 1 hour and the solver time per time step is also decreased by 20 – 25% from 47 – 50 s to 37 – 38 s. The 5 s time step size simulation then can be completed within 5.5 hours. If less accuracy is acceptable, 15 s time step size can be used and the simulation can be executed within 2 hours.

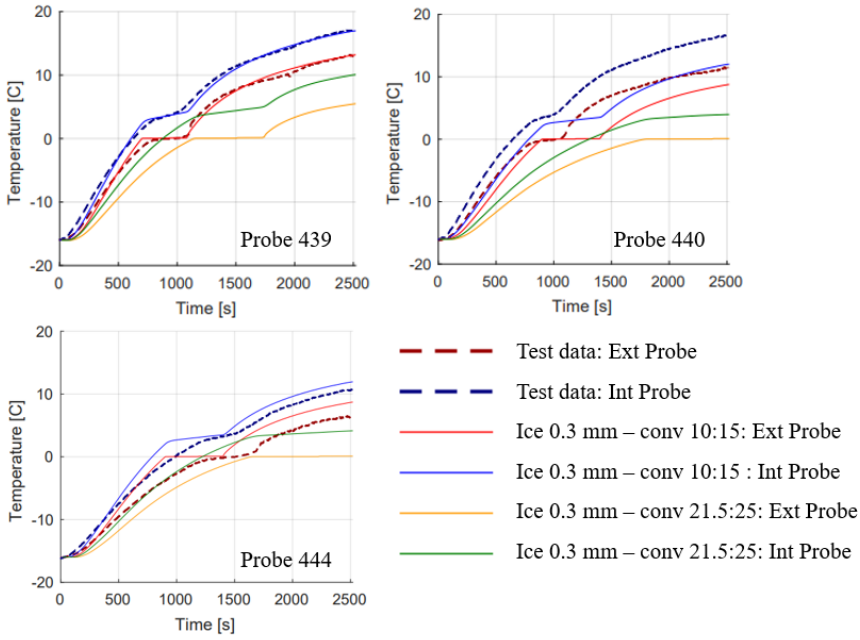

Figure 4.27 *Representative temperature profile from probes on the windscreen with HVAC velocity and turbulence profile set at defroster inlet and different HTC values set at the upper ice layer boundary in comparison with the test data.*

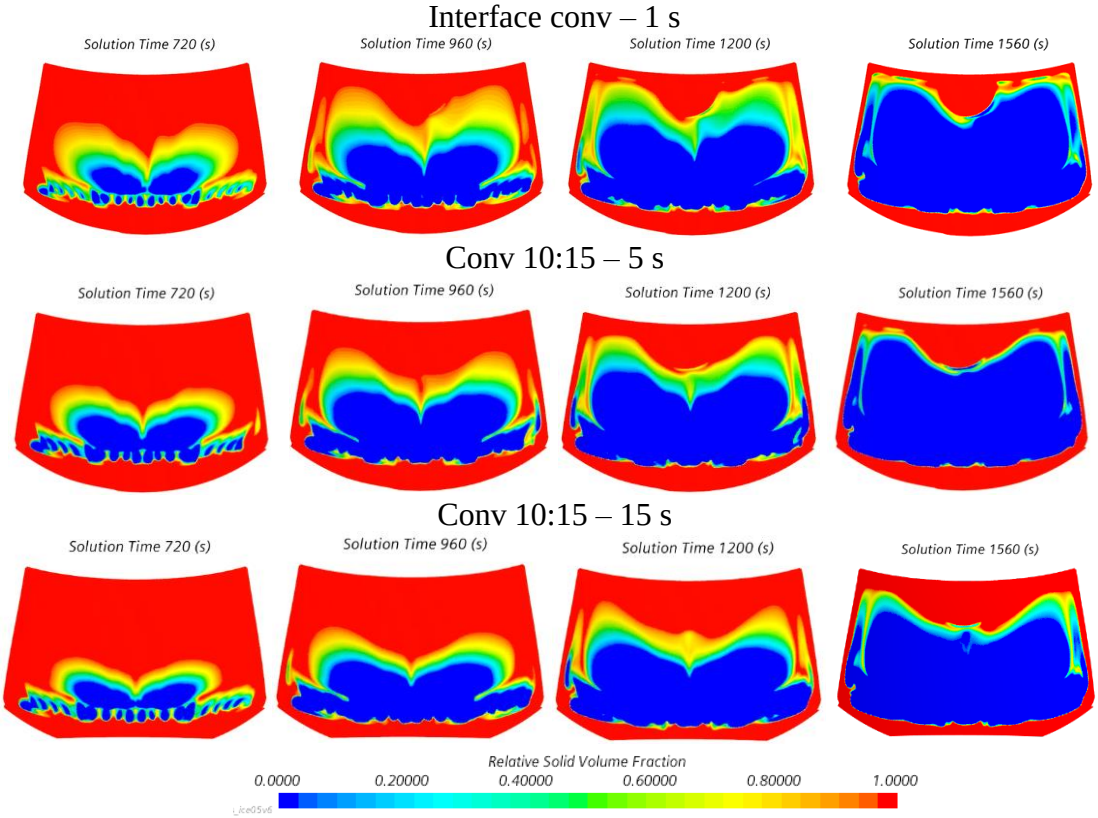

Figure 4.28 *Ice melting pattern at different testing times from simulations with HVAC velocity and turbulence profile set at defroster inlet and different thermal boundary condition set at the upper ice layer surface.*

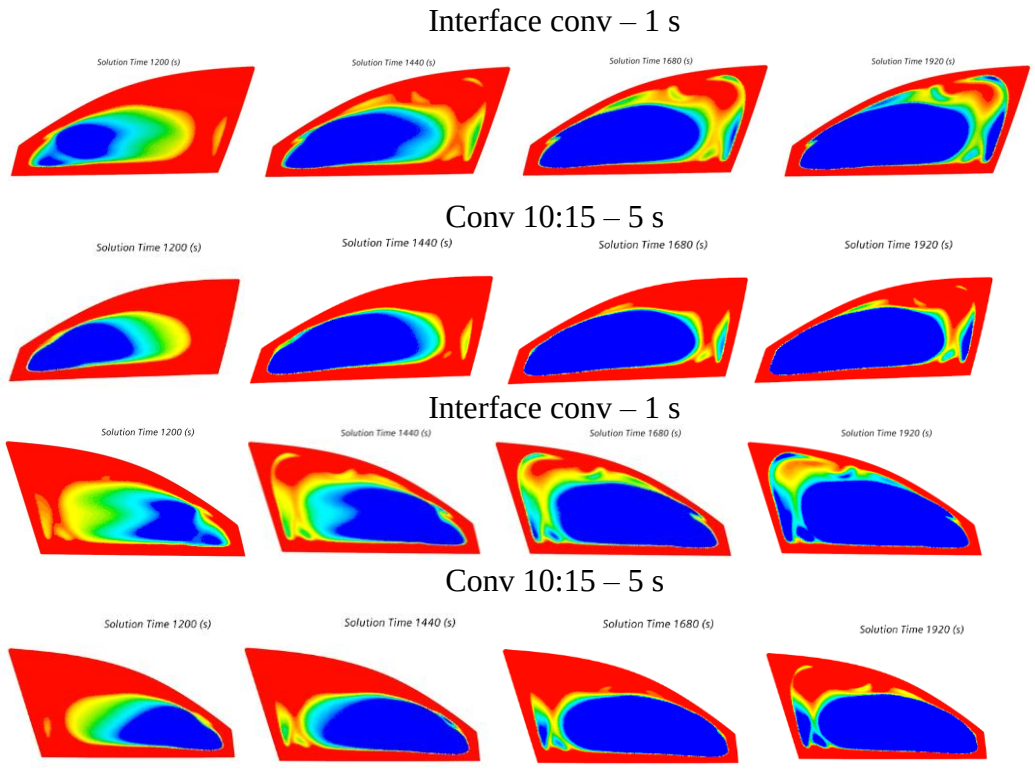

Figure 4.29 Ice melting pattern of front side windows at different testing times from simulations with HVAC velocity and turbulence profile set at defroster inlet and different thermal boundary condition set at the upper ice layer surface.

4.9 Effect of temperature-dependent material properties

The material properties of the ice and air are investigated. For the change of ice to water density, it appears that, there are only less than 1 minute melting time reduction and a weird fluctuation seen in the temperature profile in probe 438, 440, 443 and 444 as partly illustrated in Figure 4.30. This fluctuation indicates the simulation instability when the density is suddenly changed. Nonetheless, for the rest of the probes, the temperature profiles remain exactly the same. No distinct difference is seen in the ice melting pattern either. Consequently, this parameter is considered insignificant and the density can be kept constant for stability. Note that this simulation was done during the convection study so the ice thickness of 0.3 mm and the manually set HTC on the ice upper interface of 21.5:25 W/m^{2}K before and after melt are applied.

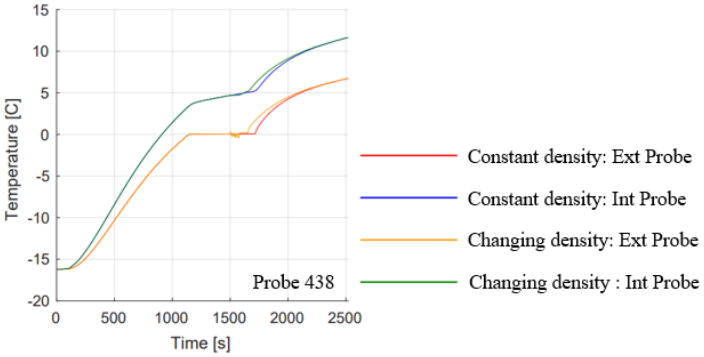

Figure 4.30 Representative temperature profile from probes on the windscreen for constant and changing density in the ice layer.

As for the air and water temperature dependent properties, the temperature profile results also show no noticeable difference as seen in Figure 4.31. It can be concluded that the temperature dependent thermal material properties are not a significant parameter here. Constant material properties are thus acceptable for the simulation.

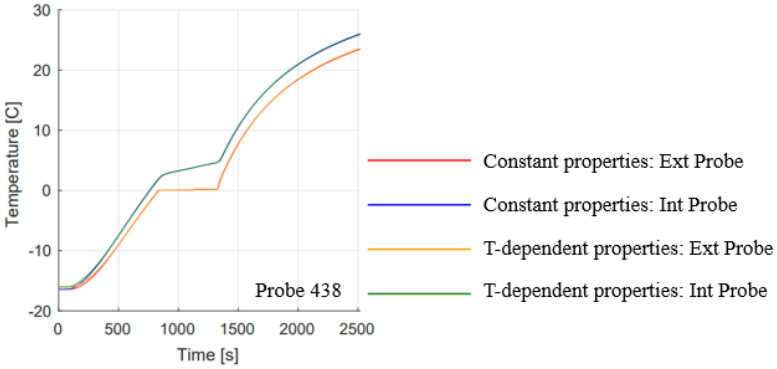

Figure 4.31 Representative temperature profile from probes on the windscreen for constant and temperature-dependent thermal properties.

4.10 Geometry verification

Different modifications of the geometry are studied in this section to examine its effect on the results. As discussed in section 4.1.1, the results from 5 s time step size simulation from other geometry modifications are closer to the time accurate result of geometry 1 (original geometry) as shown in Figure 4.32. From this, it appears that all modified geometries have less than 1-minute variation of the melting range here. Moreover, the content of melted area in each ice melting pattern also resembles each other very well as seen in Figure 4.33. Although, slight variation in the melting pattern is still seen. The pattern in geometry model 1 and 2 with original defroster inlet position are quite different from the rest with modified defroster inlet position. So, it seems the modification of the defroster inlet has more effect on this shape variation than other parameters. Nonetheless, with HVAC velocity and turbulence profile which has smoother ice melting pattern as illustrated in Figure 4.34, no significant difference is seen. Thus, overall, it can be concluded that the geometry should not be a significant issue but it will be beneficial to be aware of the possible variation. With this conclusion, it means the external car body geometry can be excluded to save the computational resource. This will avoid the increase of the solver time per time step by 10 – 15%.

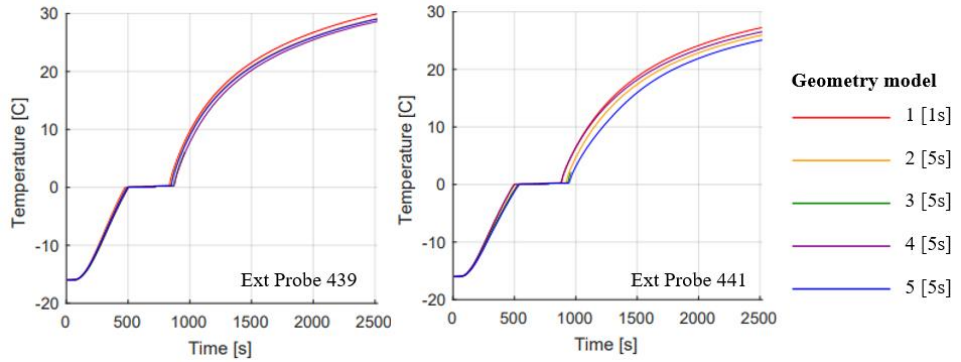

Figure 4.32 Representative temperature profile from Ext probes on the windscreen with different geometry models.

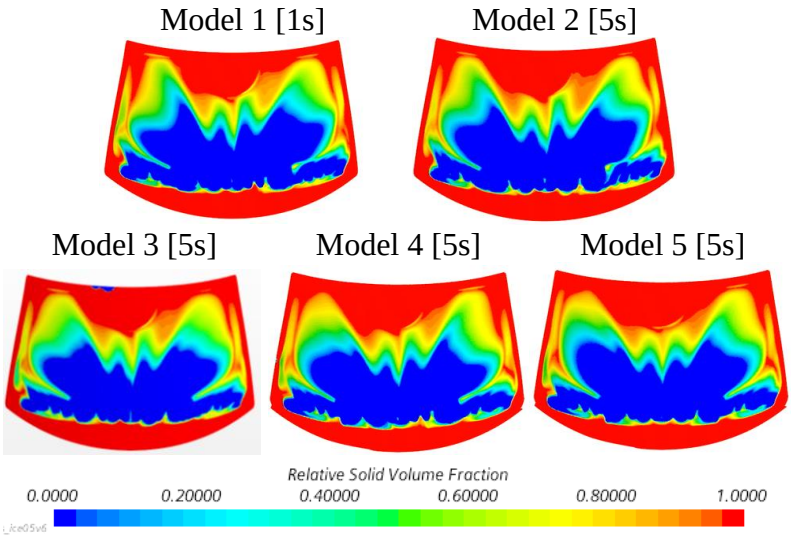

Figure 4.33 Ice melting pattern at 14 minutes testing time from simulations with different geometry models.

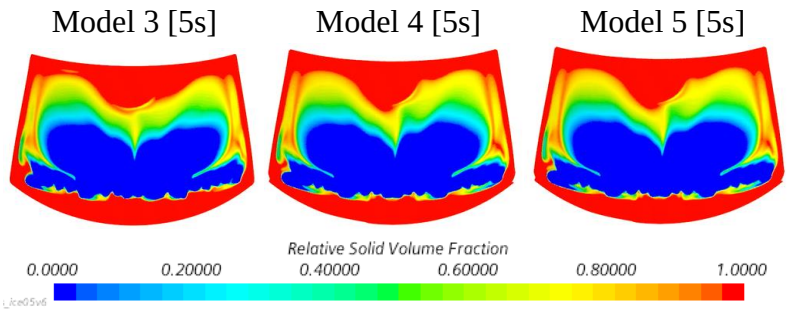

Figure 4.34 Ice melting pattern at 18 minutes testing time from simulations with velocity and turbulence profile from HVAC simulation set as defroster inlet boundary condition from different geometry models.

4.11 Final simulation scheme validation

From all previous studies, the preferable setting for each parameter is identified. Except for the time step size, defroster inlet velocity and defroster inlet temperature, the default simulation settings are applied. Since the time step size and the defroster inlet velocity lead to an interesting discussion in previous studies, they are further investigated here. 2 simulations with and without HVAC unit are executed in comparison. Due to its large mesh size, the simulation with HVAC and all air duct systems are executed at 5 s time step for the sake of efficiency. The simulation without HVAC is then executed at 2 s time step size since it is less expensive. As for the defroster inlet temperature, the T-HVAC profile from VB test is used.

The simulation results are validated solely with the ice melting pattern since it is the only available information from this test data. As demonstrated in Figure 4.35 and Figure 4.36, it can be seen that the area of melted area from both simulations are quite similar and also match well with the test data. Note that the frozen stripes on the side area on the windscreen at 25 minute-testing time are also visible on the test data if observe closely. This confirms that the flow field in this simulation is quite steady and so the results are independent of time step size. The turbulence profile from HVAC unit though does influence the shape of the melted area slightly, leading to a sharper and more accurate ice melting pattern. This confirms that both HVAC velocity and turbulence profile should be used in future application in order to yield an accurate result.

Finally, to also investigate the reliability of the tuned external convection scheme, another simulation with HVAC unit is executed following the external convection study setting with the final tuned HTC value of 10:15 W/m^2K, ice thickness of 0.3 mm and 5 s time step size. The results now surprisingly show 4 – 5 minutes early melting time compared to the results from interface convection simulations and the test data. The difference is even more apparent on the front side windows. Thus, this suggests that even though the defroster mass flow rate is constant, the HTC might still vary from other parameters, for instance of the possible difference ice thickness in each test. So, the HTC value needs to be tuned with caution for different vehicle model and test condition before it can be trusted.

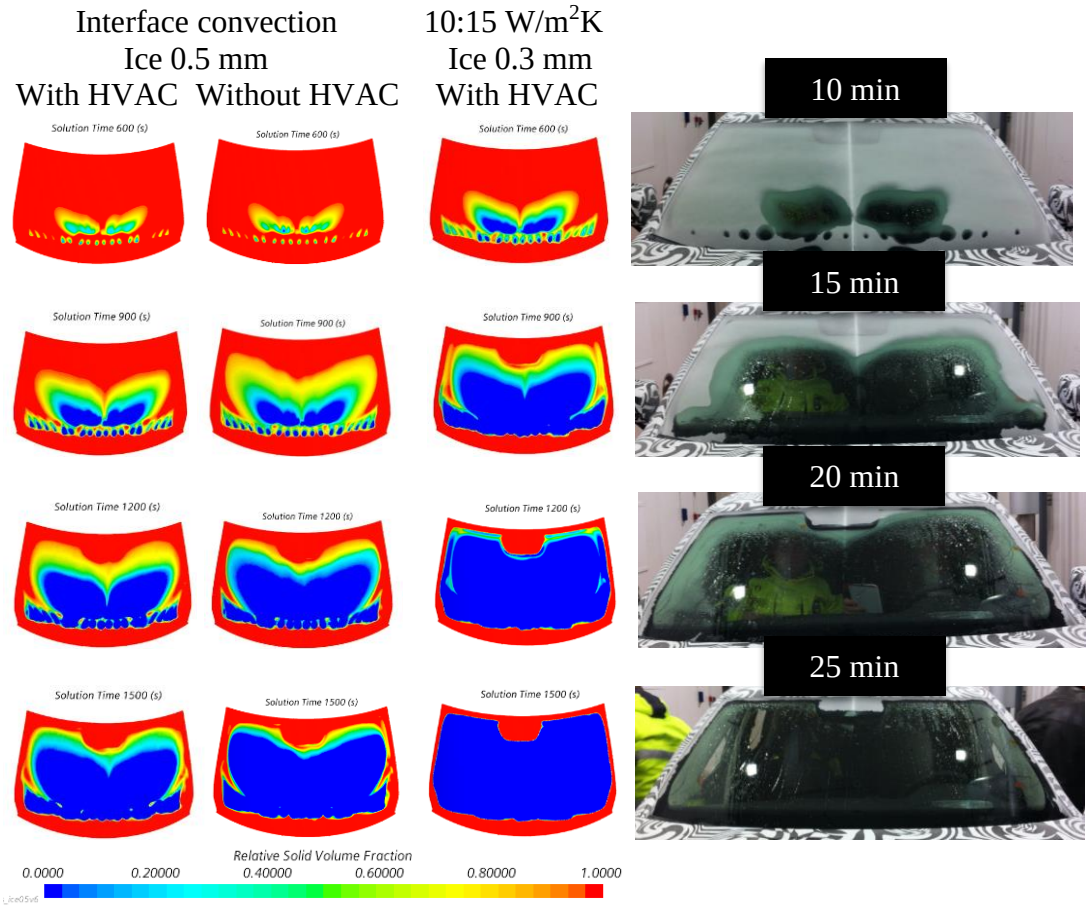

Figure 4.35 Ice melting pattern on the windscreen at different testing times from simulations with different simulation schemes and performance test.

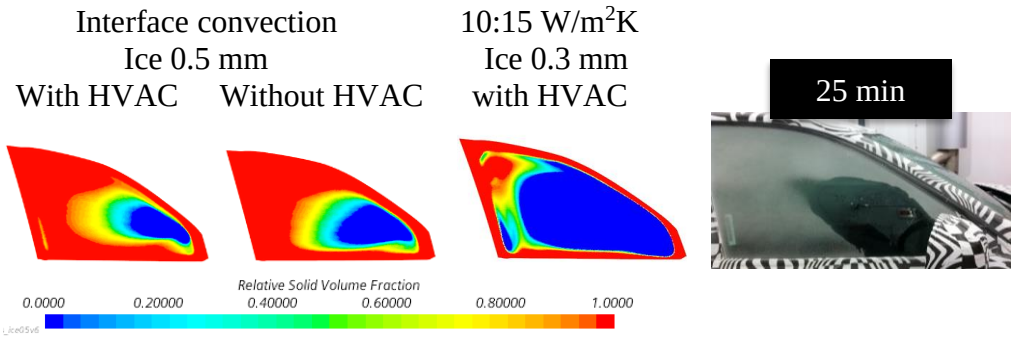

Figure 4.36 Ice melting pattern on the passenger side window at 25 minutes testing time from simulations with different simulation schemes and performance test.

4.12 Final remark on the relative solid volume fraction

The ice melting pattern in this study is illustrated with the continuous color gradient of the relative solid volume fraction scale. Now, the accurate area of clear vision in the simulation in correlation to the test data is actually not at the 0 or 1 in this scale but somewhere in between. Thus, for the ease of justification in future application, a more distinct scale is preferred. The most accurate result from the study is identified to be the one with the defroster inlet boundary condition set to HVAC velocity and turbulence profile, executed in geometry model 5 with 5 s time step size and full flow solver. This result is then validated against the test data in order to find the suitable cutoff value that will differentiate the clear vision more apparently. As illustrated in Figure 4.37, the cutoff value is suggested to be at 0.5 relative solid volume fraction. This results in relatively accurate ice melting pattern, although it is slightly delayed in the upper and side region on the windscreen. However, this is preferable since during the design phase, the risk of overestimated result should be avoided. Note that this cutoff value also works perfectly fine with the result from simulation with manually set convection rate over the ice layer from Volvo VA model as well.

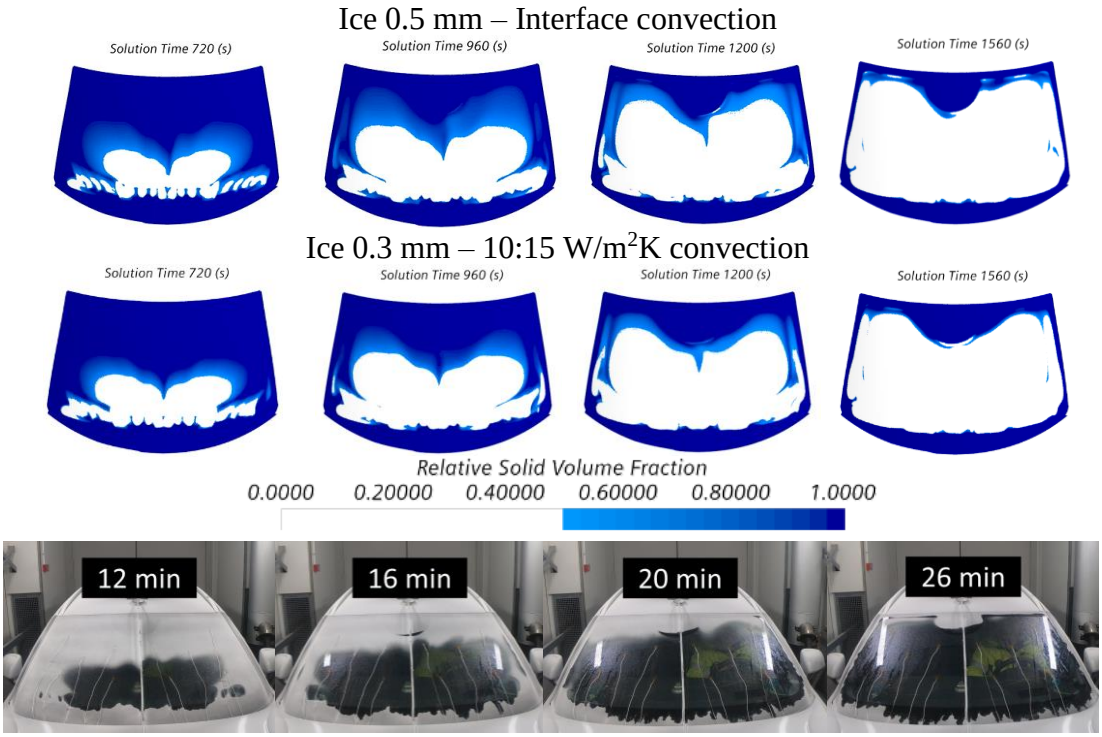

Figure 4.37 Ice melting pattern at different testing times from simulations with new color scale in comparison to the performance test on Volvo VA model.

5 Conclusion and Future Work Possibilities

Simulation scheme with satisfying result accuracy and efficiency are obtained from this study. First, a few significant parameters are identified. Mesh and prism layer setting can affect the simulation stability and efficiency greatly so it should be selected with caution. From the mesh independent study, mesh 3 with 65 million cells is found to be the optimal setting. Then, regarding the efficiency, the time step size is considered an immensely influential parameter. Since the flow field is quite steady in this system, a time step size as large as 5 s time step can be used, leading to less than 7 hours simulation time with 960 computational cores for 42 minutes testing time simulation. Although, it was noted that certain defect in some geometry can induce fluctuation and so the solution can be delayed for larger time step size. Hence, this should be verified first before use. Then, to further increase the simulation efficiency, the flow solver can be safely frozen after a steady state simulation to obtain the flow field. This can fasten the transient simulation time by 30% so it should be really useful in the design phase when a lot of simulations is to be executed. For a rough simulation, with 15 s time step size, flow solver frozen and the maximum number of iterations per time step reduced to 15, the simulation can be executed within 2 hours and still yield a fairly accurate result with only minor variation.

Next, regarding the result accuracy, a number of parameters can affect the ice melting pattern and its melting time. First, the choice of turbulence models can influence the ice melting pattern and result stability quite significantly. From the study, RKE model is still found to be most suitable for this simulation. Then, the defroster inlet velocity and especially the turbulence profile can affect the result drastically as well. Accurate profile at the HVAC-defroster connection should thus be obtained. This can be achieved from a separate steady state simulation with HVAC unit and other air duct system since including these components into the defroster simulation will increase the computational cost too significantly. Another parameter that can delay the result considerably is the ice layer thickness so this should be verified in the future test in order to increase the reliability of the simulation as well. Without any verification from the test, the 0.5 mm should be used to avoid unrealistic overestimation of the defroster performance. Finally, for the defroster inlet temperature profile, it appears that the result is not highly dependent on this parameter and a variation from 5 – 10 °C is still acceptable. Thus, there is no need to simulate the heat loss through defroster duct and the profile from previous test data can be applied as input in the future application with high certainty. Other than these, the temporal discretization scheme, gravity, temperature dependent material properties and geometry modifications are considered insignificant and default setting in this simulation can be used.

From all of these settings, the ice melting pattern yielded is highly accurate. The simulation scheme is also proved to be valid for Volvo VB as well, confirming the method reliability. However, the temperature profiles are still overpredicted in some probes for this setting. The alternative to manually set the convection rate over the ice layer is found to be useful for fixing this issue. Although the HTC value needs to be tuned with different test conditions, after it is tuned, it can yield both highly accurate temperature profiles and ice melting pattern result as well as decrease the computational time by 20 – 25% from reduced external air domain size. Thus, this scheme can be considered as another possible and valuable alternative as well.

Regarding the future work possibilities, the simulation scheme with manually set HTC value can be further improved by finding a better correlation between the defroster inlet flow rate or the impingement velocity on the internal side of the windscreen and the HTC value to allow it to be easily adjusted. In addition, this might allow the HTC to be set non-homogeneously over the windscreen as well which can help with the delay issue in some region. Finally, future work can also focus on the optimization of the defroster inlet flow and temperature in order to better optimize the energy usage as well.

References

1. Launder, B.E. and B.I. Sharma, *Application of the energy-dissipation model of turbulence to the calculation of flow near a spinning disc.* Letters Heat Mass Transfer, 1974. **1**: p. 131.
2. Jones, W.P. and B.E. Launder, *The prediction of laminarization with a two-equation model of turbulence.* International Journal of Heat and Mass Transfer, 1972. **15**(2): p. 301-314.
3. Shih, T.-H., et al., *A new k-ϵ eddy viscosity model for high reynolds number turbulent flows.* Computers & Fluids, 1995. **24**(3): p. 227-238.
4. Sarkar, S. and L. Balakrishnan, *Application of a Reynolds stress turbulence model to the compressible shear layer.* AIAA, Fluid Dynamics, 21st Plasma Dynamics and Lasers Conference, 21st, Seattle, WA, June 18-20, 1990. 17 p., 1990.
5. Rodi, W., *Experience with two-layer models combining the k-epsilon model with a one-equation model near the wall.* 29th AIAA Aerospace Sciences Meeting, 1991. **29**.
6. Wolfshtein, M., *The velocity and temperature distribution in one-dimensional flow with turbulence augmentation and pressure gradient.* International Journal of Heat and Mass Transfer, 1969. **12**(3): p. 301-318.
7. Durbin, P.A., *A Reynolds stress model for near-wall turbulence.* Journal of Fluid Mechanics, 2006. **249**: p. 465-498.
8. Manceau, R. and K. Hanjalić, *Elliptic blending model: A new near-wall Reynolds-stress turbulence closure.* Physics of Fluids, 2002. **14**(2): p. 744-754.
9. Lardeau, S. and F. Billard, *development of an elliptic-blending lag model for industrial applications*. 2016.
10. Revell, A., et al., *A Stress-Strain Lag Eddy Viscosity Model for Unsteady Mean Flow.* International Journal of Heat and Fluid Flow, 2006. **27**: p. 821-830.
11. Kolmogorov, A.N. *Equations of turbulent motion in an incompressible fluid*. in *Dokl. Akad. Nauk SSSR*. 1941.
12. Wilcox, D.C., *Turbulence modeling for CFD*. Vol. 2. 1998: DCW industries La Canada, CA.
13. Menter, F.R., *Two-equation eddy-viscosity turbulence models for engineering applications.* AIAA Journal, 1994. **32**(8): p. 1598-1605.
14. Durbin, P., *Technical Note On the k-3 stagnation point anomaly.* International Journal of Heat and Fluid Flow, 1996. **17**(1): p. 89-90.
15. Sarkar, S., et al., *The analysis and modelling of dilatational terms in compressible turbulence.* Journal of Fluid Mechanics, 2006. **227**: p. 473-493.
16. Reichardt, H., *Vollständige Darstellung der turbulenten Geschwindigkeitsverteilung in glatten Leitungen.* ZAMM - Journal of Applied Mathematics and Mechanics / Zeitschrift für Angewandte Mathematik und Mechanik, 1951. **31**(7): p. 208-219.
17. Siple, P.A. and C.F. Passel. *Measurements of dry atmospheric cooling in subfreezing temperatures*. 1945.
18. Bergman, T.L., et al., *Fundamentals of Heat and Mass Transfer*. 2011: Wiley.
19. Jongen, T., *Simulation and modeling of turbulent incompressible fluid flows*. 1998, EPFL.

Appendix

Model coefficients

The values for model coefficients used in the turbulence models and wall function are listed in Table A and Table B.

Table A Model coefficients for turbulence models.

k-epsilon		k-epsilon Lag EB		k-omega	
$C_{\varepsilon 1}$	$\max\left(0.43, \frac{\eta}{\eta+5}\right)$ where $\eta = \frac{\lvert\bar{S}\rvert k}{\varepsilon}$	$C_{\varepsilon 1\mathrm{LEB}}$	1.44	C_{β}	0.075
$C_{\varepsilon 2}$	1.9			C_{β^*}	$0.09 + 0.135\max(0, M_t^2 - 0.0625)$
$C_{\varepsilon 3}$	$\tanh\frac{\lvert v_{\parallel g}\rvert}{\lvert v_{\perp g}\rvert}$			$C_{\beta KO}$	$0.0828 - 0.0078F_1 - 0.135\max(0, M_t^2 - 0.0625)$
		C_{η}	75	C_{γ}	$0.4404 + 0.1128F_1$
$C_{\sigma k}$	1	$C_{\sigma\varphi}$	1	$C_{\sigma k-\mathrm{KO}}$	$1 - 0.15F_1$
$C_{\sigma\varepsilon}$	1.2			$C_{\sigma\omega}$	$0.856 - 0.356F_1$
C_{μ}	0.09	$C_{\mu LEB}$	0.22	$C_{\sigma\omega 2}$	0.856
C_l	$0.42C_{\mu}^{-3/4} = 2.556$	C_k	203	C_{a1}	0.31
C_M	2	C_L	0.164		
C_t	1	C_{tLEB}	4		

Table B Model coefficients for wall function.

C_{κ}	0.42 [von Karman constant]
C_{Γ}	$\frac{0.01(\mathrm{Pr}y^+)^4}{1+5\mathrm{Pr}^3y^+}$
C_b	$\frac{1}{2}\left(C_{ym}\frac{C_{\kappa}}{C_w} + \frac{1}{C_{ym}}\right)$
C_E	9 [log law offset]
C_{Pr}	$9.24\left[\left(\frac{\mathrm{Pr}}{\mathrm{Pr_t}}\right)^{\frac{3}{4}} - 1\right]\left[1 + 0.28\exp\left(-0.007\frac{\mathrm{Pr}}{\mathrm{Pr_t}}\right)\right]$
C_w	$\frac{1}{C_{\kappa}}\ln\left(\frac{C_E}{C_{\kappa}}\right) = 7.297$
C_{ym}	$\max\left(3,\ 267(2.64 - 3.9C_{\kappa})\right){C_E}^{0.0125} - 0.987$

Model functions

Model functions for turbulence models and wall function are provided in this section.

RKE Turbulence model

1. Damping factor f_2

$$f_2 = \frac{k}{k+\sqrt{\nu\varepsilon}} \tag{i}$$

2. Wall proximity indicator [19]

$$f_\lambda = \frac{1}{2}\left[1 + \tanh\left(\frac{Re_d - Re_y^*}{A}\right)\right] \tag{ii}$$

where $\Delta Re_y = 10$, $Re_y^* = 60$ and $A = \frac{|\Delta Re_y|}{\operatorname{atanh} 0.98}$

Re_y^* denotes a model coefficient specifying the limit of applicability of the two-layer formulation, while A determines the width of f_λ so that its value is within 1% of its far-field value.

3. Damping function for realizability near the wall f_μ

$$f_\mu = \frac{1}{C_\mu\left\{4+\sqrt{6}\cos\left[1-3\cos^{-1}\left(\sqrt{6}\frac{S^{*3}}{\sqrt{S^*:S^{*3}}}\right)\right]\frac{k}{\varepsilon}\sqrt{\bar{\mathbf{S}}:\bar{\mathbf{S}}+\bar{\mathbf{W}}:\bar{\mathbf{W}}}\right\}} \tag{iii}$$

where $\bar{\mathbf{W}} = \frac{1}{2}(\nabla\bar{v} - \nabla\bar{v}^T)$

$\bar{\mathbf{S}} = \frac{1}{2}(\nabla\bar{v} + \nabla\bar{v}^{\mathrm{T}})$

$S^* = \bar{\mathbf{S}} - \frac{1}{3}\mathrm{tr}(\bar{\mathbf{S}})\mathbf{I}$

and tr() is a trace matrix.

LEB KE Turbulence model

1. Damping function f_W

$$f_W = -\left(C_{\varepsilon 2} + 4 - \frac{1}{C_{\mu Leb}}\right)\frac{\varphi}{t_{te}} \tag{iv}$$

2. Damping function f_h

$$f_h = -\frac{1}{t_{te}}\left(C_1 + C_{\varepsilon 2} - 2 + C_1^*\frac{G_k+G_b}{\rho\varepsilon}\right)\varphi + \frac{C_{P3}}{t_{te}} + \frac{C_3^*}{\sqrt{2}}\varphi|\bar{\mathbf{S}}| +$$

$$\frac{1}{|\bar{\mathbf{S}}|^2 t_{te}}\left[\frac{2}{C_{\mu Leb}}(1-C_4)\mathrm{A}\bar{\mathbf{S}} - \frac{2}{C_{\mu Leb}}(1-C_5)\mathrm{A}\widehat{\mathbf{W}}\right]:\bar{\mathbf{S}} \tag{v}$$

where $\mathrm{A} = -2\frac{\mu_t}{\rho k}\left[\bar{\mathbf{S}} + \frac{2-2C_5}{C_1+C_1^*+1}\frac{2}{\sqrt{(\bar{\mathbf{S}}+\widehat{\mathbf{W}}):(\bar{\mathbf{S}}+\widehat{\mathbf{W}})}}\left(\bar{\mathbf{S}}\widehat{\mathbf{W}} - \widehat{\mathbf{W}}\bar{\mathbf{S}}\right)\right]$

$\widehat{\mathbf{W}} = \bar{\mathbf{W}} - \mathbf{W}^{\mathbf{S}}$

$$\mathbf{W^S} = \frac{1}{|\bar{\mathbf{S}}|^2}\left(\bar{\mathbf{S}}\frac{D\bar{\mathbf{S}}}{Dt} - \frac{D\bar{\mathbf{S}}}{Dt}\bar{\mathbf{S}}\right)$$

$$C_{P3} = \frac{f_{\mu Leb}}{C_{\mu Leb}}\left(\frac{2}{3} - \frac{C_3}{2}\right)$$

$$f_{\mu Leb} = \frac{|\bar{\mathbf{S}}|t_{te}+\alpha^3}{\max(|\bar{\mathbf{S}}|t_{te},1.87)}$$

and C_1, C_1^*, C_3, C_3^*, C_4, C_5 = 1.7, 0.9, 0.8, 0.65, 0.625, 0.2 respectively.

A denotes the Reynolds-stress anisotropy tensor, while $\widehat{\mathbf{W}}$ and $\mathbf{W^S}$ denote the modified absolute vorticity tensor and Spalart-Shur tensor respectively. Finally, $C_{P3}$is a damping function implementing the kinematic blocking of the wall.

SST KO Turbulence model

1. Blending function F_1

$$F_1 = \tanh\left(\left[\min\left(\max\left(\frac{\sqrt{k}}{C_{\beta^*}\omega y}, \frac{500\nu}{y^2\omega}\right), \frac{2k}{y^2 CD_{k\omega}}\right)\right]^4\right) \quad \text{(vi)}$$

2. Cross diffusion coefficient $CD_{k\omega}$

$$CD_{k\omega} = \max\left(\frac{1}{\omega}\nabla\cdot\omega\ \nabla\cdot k, 10^{-20}\right) \quad \text{(vii)}$$

Wall function

1. Blending function f_γ

$$f_\gamma = \exp\left(-\frac{Re_d}{11}\right) \quad \text{(viii)}$$